Title: Tsunamigenic earthquake simulations using experimentally derived friction laws

S. Murphy[1,2*], G. Di Toro[3,4], F. Romano[1], A. Scala[1], S. Lorito[1], E. Spagnuolo[1], S. Aretusini[3], G. Festa[5], A. Piatanesi[1], S. Nielsen[6]

[1]Istituto Nazionale di Geofisica e Vulcanologia, Rome, Italy

[2]Ifremer, Plouzané, France

[3]University of Manchester, Manchester, United Kingdom

[4]Università degli Studi di Padova, Padua, Italy

[5]Università di Napoli Federico II, Naples, Italy

[6]Durham University, Durham United Kingdom

*shane.murphy@ifremer.fr

Keywords: subduction zone; megathrust; dynamic rupture; rock physics experiments; tsunami earthquake

Abstract

Seismological, tsunami and geodetic observations have shown that subduction zones are complex systems where the properties of earthquake rupture vary with depth as a result of different pre-stress and frictional conditions. A wealth of earthquakes of different sizes and different source features (e.g. rupture duration) can be generated in subduction zones, including tsunami earthquakes, some of which can produce extreme tsunamigenic events. Here we offer a geological perspective on these depth-dependent features. Subduction zone fault rocks are dominantly incohesive and clay-rich near the surface, transitioning to cohesive and more crystalline at depth.

We combine a lithology-controlled, depth-dependent experimental friction law with elastodynamic rupture simulations for a Tohoku-like subduction zone. By using simplified pre-stress distributions, we show that by shifting along fault dip the location of the high shear stress regions ("asperities"), moderate to great thrust earthquakes and tsunami earthquakes are produced, consistent with seismological, geodetic, and tsunami observations. Central to this depth dependence is that slip is confined to the high stress asperity at depth; near the surface rupture is impeded by the rock-clay transition constraining slip to the clay-rich layer. However, when the high stress asperity is located in the clay-to-crystalline rock transition, great thrust earthquakes can be generated similar to the M_w 9 Tohoku (2011) earthquake.

1. Introduction

Seismological, geodetic, and tsunami observations have shown that subduction zones are complex systems where the properties of earthquake rupture vary with depth (Lay et al., 2012). For example, earthquake duration normalized for event size has been observed to decrease with depth; this recurrent feature has been attributed to depth varying shear modulus and / or stress drop for individual earthquakes (Bilek and Lay, 1999; Bilek et al., 2016; Geist and Bilek, 2001). Depth variation in subduction ruptures is for example evident when comparing the different historical earthquakes that occurred off the Pacific coast of Tohoku region in Japan (Fig. 1). A number of major (M_w 7-7.9) thrust earthquakes mostly slipped within a depth range of 10 – 40 km. These events involved individual patches of concentrated slip implying the breaking of at least one prominent, high stress asperity (Shao et al., 2011; Yamanaka and Kikuchi, 2004). Conversely, the 1896 Meiji event (M 8.2 – 8.4), likely

50 involved slip primarily at the base of the shallow accretionary wedge or beneath it.
51 This earthquake produced a disproportionately large tsunami relative to its moment
52 magnitude, possibly making it a potential 'tsunami earthquake' (Kanamori, 1972).
53 The great M_w 9.0 2011 Tohoku earthquake nucleated at ~20 – 25 km depth, and
54 produced slip at traditionally expected depths while also realising a substantial
55 amount of slip all the way to the trench (i.e., at less than 10 km depth) (Chu et al.,
56 2011; Ide et al., 2011; Romano et al., 2014).

57 Numerical models of the dynamic rupture process have successfully described
58 either individual types of earthquakes, for example the Tohoku event (Kozdon and
59 Dunham, 2013; Noda and Lapusta, 2013), or both thrust and tsunami earthquakes in
60 the same model (Mitsui and Yagi, 2013). Numerical models coupled with the rate-
61 and-state friction law have been used to reproduce full seismic cycles for subduction
62 environments. However, this comes at the expense of either failing to account for
63 geometry / free surface effects and inhomogeneity in the material surrounding the
64 fault (Cubas et al., 2015; Noda and Lapusta, 2013), or by simplifying wave
65 propagation to static stress changes on the fault plane (Shibazaki et al., 2011). Fully
66 dynamic simulations including a free surface and variable geometry have tended to
67 focus on specific rupture features of the Tohoku earthquake such as the slip in the
68 trench or long period guided wave propagation in the ocean (Hirono et al., 2016;
69 Huang et al., 2013; Kozdon and Dunham, 2014). Depth dependent changes in
70 frictional parameters have been parameter tested using rate-and-state models for the
71 2011 Tohoku (Kozdon and Dunham, 2013). However, to our knowledge, no
72 numerical model has been able to reproduce a range of different observed earthquakes
73 types (e.g. Fig. 1) while at the same time accounting for the fault zone geology as
74 proposed here. The focus of this study is to provide a simple model that reconciles the

different observed earthquake types with fault properties from independent theoretical and laboratory studies. We investigate the detail of rupture dynamics due to depth-dependent frictional conditions focusing on a specific time window of the seismic cycle including the sub-seismic frictional properties of the fault materials (Hartog et al., 2012). Investigating inter-seismic and nucleation processes are beyond the scope of this study. As a consequence, the set up for the numerical model (e.g., type of friction law, initial stress distribution) was chosen based on geological and geophysical (though limited) constraints and with the aim of investigating how dynamic rupture features of an earthquake vary when using a geological consistent model and how these differences compare with observed earthquake types.

2. Numerical Model

We modelled the earthquake rupture dynamics (Festa and Vilotte, 2005) on a 2D cross-section through a Tohoku-like fault (Figs. 2a-d). Dynamic rupture is simulated using a 2D non-smooth spectral element method (Festa and Vilotte, 2005). The curved fault geometry is based on Slab 1.0 (Hayes et al., 2012) which has been slightly modified so that the subduction interface extends to the surface. The media is heterogeneous with the layers and their elastic properties (described in Fig. 2 and Table S1 in *Supplementary Material*) based on a seismic survey in the zone of the 2011 Tohoku earthquake (Miura et al., 2005).

2.1 Laboratory derived thermal weakening friction law

A slip weakening empirical friction law was used in all simulations which is particularly suitable for representing dynamic weakening observed in a regime of slip velocities that rapidly accelerate to seismic slip rates. This law is based on laboratory

observations of the evolution of friction with slip in a rotary shear machine where cohesive (serpentinites, peridotites, gabbros, basalts, marbles, granitoids, sandstones, etc.) and non-cohesive (clay-rich gouges, serpentinite gouges, basalt gouges, etc.) rocks were tested over a quite large range of slip rates (0.1 to 6.5 m/s), accelerations (0.5 to 65 m/s^2), normal stresses (5 to 95 MPa), ambient conditions (room humidity to fluid saturated) and displacements (0.3 to 50 m) expected during moderate to large earthquakes (Di Toro et al., 2011). A common feature from this extensive set of experiments is that the evolution of friction with slip can be described by an exponential decay to a first order approximation. This dependency is defined as:

$$\mu\,(\delta) = \mu_d + (\mu_s - \mu_d)e^{\frac{-\delta}{d_{th}}} \qquad \text{(Eq. 1)}$$

where μ_s and μ_d are the static and dynamic friction coefficients respectively and depend on material type. The co-seismic slip is δ and d_{th} the thermal weakening distance. For a suite of experiments performed at a variety of slip rates and normal stresses, d_{th} was shown to have an inverse relationship with the normal stress σ_n:

$$d_{th} = \alpha\,\|\sigma_n\|^{-\beta} \qquad \text{(Eq. 2)}$$

with α ranging between 3 - 78 depending on material type (Di Toro et al., 2011) and β = 1 (Nielsen et al., 2010). This thermal weakening friction law produces a similar exponential evolution of fault strength with slip to that observed by Hirono et al. (2016) whose numerically modelled thermal pressurization on the Japan Trench using expected permeability and porosity for the region. There are a number of other empirical friction laws (e.g., linear slip weakening (Ida, 1972); rate-and-state

125 (Dieterich, 1979; Ruina, 1983)). We have chosen the thermal weakening friction law
126 as it is based on rock physics experiments performed at slip-rates expected during
127 large earthquakes using materials typical in subduction zones.
128
129 ***2.2 Variation in fault material***
130 Depth dependent frictional parameters were chosen based on expected
131 dominant rock types in mega-thrust environments (Hacker et al., 2003a; 2003b;
132 Kimura et al., 2012; Meneghini et al., 2010). Initially unconsolidated and, in the case
133 of Tohoku, clay-rich sediments (Chester et al., 2013), undergo compaction,
134 dehydration, diagenesis and metamorphism into crystalline rocks (phyllites, schists,
135 calc-schists, marbles, quartzites, etc.) due to increasing pressure and temperature
136 during burial (Hacker et al., 2003b; 2003a; Hyndman et al., 1997; Ikari et al., 2007;
137 Kimura et al., 2012). Consequently, high velocity experiments on peridotite (Del
138 Gaudio et al., 2009) were taken as a proxy for mantle rock (i.e., μ_s = 0.7, μ_d = 0.25, α
139 = 78), however gabbro, basalts and serpentinite have similar frictional properties
140 when sheared under seismic deformation conditions (Niemeijer et al., 2011; Proctor et
141 al., 2014; Violay et al., 2014). For clay-like material the static and dynamic
142 coefficients of friction were set to 0.25 and 0.1 respectively based on experiments
143 performed under room humidity conditions and in the presence of liquid water
144 (Remitti et al., 2015; Sawai et al., 2014; Ujiie et al., 2013). Experimental studies from
145 literature were used to determine the α value used for the clay-like material in the
146 numerical model (see Fig 3 and Table S3 in Supplementary Material). Most of the
147 latter experiments were performed at room humidity on a variety of different clay
148 minerals and under increasing normal stresses. Ideally, data from experiments on
149 unconsolidated wet clay materials would be used. However, experiments at high

150 normal stress (> 20 MPa) are very challenging on these materials and not enough data
151 exist to calculate the variation of d_{th} with normal stress. Setting $\beta = 1$ based on
152 theoretical findings (Nielsen et al., 2010), $\alpha = 3.712$ provided the best fit for
153 equation 2 to the experimental data (see Fig. 3) with a R-square of 0.735 and a 95%
154 confidence bounds of 3.32 to 4.11. Below 40 km d_{th} was artificially increased to 20 m
155 in order to act as a numerical barrier to rupture at the bottom of the fault. This depth
156 was chosen as it corresponds to the depth at which co-seismic slip in the 2011 M_w 9.0
157 Tohoku earthquake rapidly decreased and the largest post-seismic slip occurred
158 (Ozawa et al., 2011). This is also the estimated depth where creep begins (Freed,
159 2005).

160 Using an effective basal friction of 0.03, thermal modelling of the Tohoku
161 fault (Kimura et al., 2012) places the 50°C isotherm at 10 km depth and 150°C
162 isotherm at a depth of 20 km. Guided by these findings, we defined the frictional
163 parameters above 2 km as clay-like, with a linear transition to rock-like frictional
164 parameters in the 12-20 km depth range. This interval accounts for peak dehydration
165 due to opal to quartz and smectite to illite conversion rates, estimated to occur at 12
166 km depth (Kimura et al., 2012). This transformation is consistent with experimental
167 findings on clays that showed only a minor increase in the coefficient of friction as a
168 function of smectite-to-illite transformation and effective normal stress (i.e. from 0.27
169 to 0.4) (Saffer et al., 2012). However, there is a significant increase in the friction
170 coefficient associated with a decrease in water content (e.g. by dehydration), or an
171 increase in quartz content in the system (e.g. by silicization and/or precipitation of
172 quartz veins) (Ikari et al., 2007).

173

174 ***2.3 Bi-material fault surface***

The subduction interface is on the boundary between the oceanic lithospheric layer and various hanging-wall materials (e.g., wedge and various mantle layers that vary with depth) which can lead to ill-posedness and numerical instability in terms of modelling due to the bi-material propagation (Cochard and Madariaga, 1996). To accommodate for this, the evolution of the normal stress is regularized whereby the frictional strength depends on the evolving normal stress σ_e that, in turn, varies due to normal stress perturbations σ_n depending on either a slip-rate-based or a constant characteristic time scale (Rubin and Ampuero, 2007):

$$\frac{d\sigma_e}{dt} = \frac{\alpha_e|v| + v^*}{\delta_D}(\sigma_n - \sigma_e) \qquad \text{(Eq. 3)}$$

where v^* is a characteristic slip rate, δ_D a characteristic slip scale, $|v|$ is the local value of slip rate, and α_e can assume the values 0 or 1. For this study, $v^* = 0$, $\alpha_e = 1$, and $\delta_D = 0.3\, d_{th}$ were used as they were found to produce numerically stable and physically convergent solutions (Scala et al., 2017). The relationship between the classical slip weakening distance, d_c and the thermal weakening distance, d_{th}, is $d_c \approx 3d_{th}$ (Di Toro et al., 2011).

2. 4 Presence of fluids

In order to account for the effect of fluids we consider the dynamic Coulomb wedge theory (Wang and Hu, 2006) which proposes that fluid pressure ratio, λ, and effective basal friction, defined as $\mu_b' = \mu(1-\lambda)$ (Wang et al., 2010) where μ is the coefficient of friction, vary between the front, middle and back of the forearc prism. Based on analysis of seismic profiles and thermal models (Kimura et al., 2012), λ =

0.9 was applied to the section of the fault at the back of the prism with λ = 0.95 (depth > 14.6 km) for the middle section of the prism (depth range of 9.6 – 14.6 km). For the frontal section of the prism (< 9.6 km), λ = 0.65 was used. Assuming that μ is similar to the static friction coefficient used in our dynamic simulations (i.e., $\mu = \mu_s$) we can compare our initial conditions with other studies. The initial conditions for our numerical model exhibits μ_b' of 0.0875, 0.0125 and 0.025 to 0.07 for the front, middle and back sections of the accretionary wedge which is comparable to observations (i.e., > 0.08, < 0.03 and 0.03 for the respective sections of the prism) (Kimura et al., 2012) and $\mu_b' = 0.025$ for the whole fault (Gao and Wang, 2014). Using this depth dependent λ, the principal vertical component of stress was estimated as the difference between lithostatic normal load and hydrostatic pore pressure using the principal vertical stress $\sigma_3 = (1 - \lambda) g\, \rho\, z$, where g is the gravity, ρ is the density and z is the depth. The fluid retention depth, Z_{FRD}, is the point at which fluid pressure increases at the same rate as the lithostatic gradient (Suppe, 2014). It defines the strength of the fault at depth: the deeper Z_{FRD} is, the stronger the fault becomes, and if all other parameters are similar, the larger the potential stress drop could be during rupture below Z_{FRD}. We assumed Z_{FRD} ~12 km, the point at which the transformation of the frictional parameters from clay-like to rock-like has ended. Therefore, σ_3 tracks the lithostatic gradient below z_{FRD}. The horizontal principal stress, σ_1, was set to 4.05 σ_3 (see Section A2 in *Supplementary Material* on discussion on choice for this scaling factor). The effective normal stress on the fault is calculated based on fault geometry relative to the two principal components of stress. The fault strength, that is the stress at which the fault fails, is a function of the static friction coefficient and the effective initial normal stress (black dashed line in Fig. 4a).

2.5 Initial shear stress distribution

In reality, the initial shear stress on the fault plane varies both temporally and spatially. It is dependent on a number of phenomena such as loading rate, coupling, and historical earthquakes (Nalbant et al., 2013). As discussed in the introduction, many of the historical thrust earthquakes in the Tohoku region (Fig. 1), can be described with one patch of significant slip suggesting that only one major high shear stress "asperity" failed at the yield stress in these events. Therefore, as a simplification, a single high stress asperity model is used where the initial stress is spatially concentrated in different locations along the fault plane. In order to control the location of the high stress asperity the initial shear stress distribution was generated by taking the spatial derivative of a 1D slip distribution constructed using a composite source model (Murphy et al., 2016). The location of the high stress asperity is placed randomly on the fault plane for each simulation. The maximum allowable shear stress in the model is defined by the fault strength, meaning that asperities in the crystalline rock material contain higher stress compared with asperities in clay-like material. Nucleation is achieved by lowering the effective normal stress such that the fault strength is few percent below the initial shear stress (see Fig. S2 in *Supplementary Material* for examples). The location of the nucleation is randomly chosen to be within the asperity on the fault.

3. Results

Initially, three separate simulations with asperity locations at different depths were chosen (15 km, 19 km and 36 km) as a case study (Fig. 4a). These three simulations are referred to as "shallow" (blue), "intermediate" (orange) and "deep" (purple) in reference to the relative location of the three asperities. Later this

procedure is extended to 45 simulations with asperity locations randomly chosen between 10 - 40 km depth.

3.1 Breakdown Energy

The three simulations produce radically different slip distributions (Fig. 4b): the deep asperity produced a concentrated patch of slip (maximum slip of 16 m), the intermediate asperity produced the largest earthquake (maximum slip of 38 m) with surface rupture while the shallow asperity produced the smallest earthquake (maximum slip of 9.5 m). The differences in the amount of slip and earthquake size can be traced back to the depth variation of the fault strength (Fig. 4a) and its evolution with slip (Fig. 4c). This depth dependence in turn plays an important role in controlling the interplay between the release of stored elastic energy and breakdown energy, G_b^i. The breakdown energy G_b^i has been calculated by numerically integrating the evolution of shear stress over the slipping distance using the formula (Abercrombie and Rice, 2005):

$$G_b^i = \int_0^{\delta} [\tau(\delta') - \tau(\delta)\,]d\delta' \qquad \text{(Eq .4)}$$

where δ is the total slip. The G_b^i was calculated of each point on the fault where co-seismic slip occurs in the three case studies depicted in Fig 4. The resistance to rupture dramatically increased below 17 km depth by at least a factor of 50 as shown in Fig. 5a.

3.2 Energy Release Rate

The stress drop, $\Delta\sigma$, systematically increased from 4 MPa to 20 MPa with increasing depth (Fig. 5b). The static stress drop has been calculated using $\Delta\sigma = \tau_o -$

τ_f where τ_f is the shear stress at the end of rupture and τ_o is the initial shear stress (Kato, 2012). Negative stress drop may occur (as is the case in Fig. 5b) when the stress at a point on the fault is higher at the end of the simulation than at the start. This can occur beyond the arrest region of the earthquake where fault strength does not evolve to residual dynamic strength and therefore the stress in this zone is at a higher level relative to before the earthquake. Negative stress drops may also occur when the initial stress is less than the dynamic strength of the fault ($\tau_o < \mu_d \sigma_n$), in such cases rupture can continue to propagate in these unfavourable zones for a limited distance depending on the energy release rate and G_b^i (Kozdon and Dunham, 2013).

Taking the square of the static stress drop as a proxy for the energy release rate ($G^* \propto \Delta\sigma^2$, assuming rupture velocity remains constant (Nielsen et al., 2016)), this latter quantity increased by a factor of 25 with depth. This depth-dependent relative difference between G_b^i and G^* made it difficult for rupture to propagate out of the trench zone. Therefore, earthquakes that nucleate in shallower clay-rich lithology are more likely to propagate along strike rather than down-dip producing the large length-to-width ratios observed for tsunami earthquakes (e.g., 1896 Meiji (Tanioka and Satake, 1996), 1992 Nicaragua (Ihmlé, 1996), 2006 Java (Ammon et al., 2006)).

3.3 Shallow earthquakes

Comparing the deepest and shallowest nucleating earthquakes in Fig. 4a, the latter has a longer duration (Fig. 6a) and comparable tsunami source amplitude (Fig. 6b and Section A3 in *Supplementary Material*) despite being smaller in size; these findings make the shallowest event in principle compatible with a tsunami earthquake (Satake and Tanioka, 1999). Additional simulations reveal that earthquakes with centroid depth (i.e., the average depth of the slipping area of the earthquake weighted

300 by the slip) located in the high pore pressure zone under the accretionary wedge had
301 consistently longer normalized rupture durations (duration of earthquake has been
302 normalized with respect to moment, see Section A4 in *Supplementary Material*) when
303 compared with earthquakes from other zones on the fault (Fig. 7a). This is a
304 systematic feature in our simulations and it is also consistent with seismological
305 observations (Bilek and Lay, 1999). This depth dependent variation of rupture
306 duration is due to a decrease in both the average stress drop and rigidity (Figs. 7b-c) at
307 shallow depths confirming the hypothesis that rupture duration is linked with depth
308 varying mechanical properties (Bilek and Lay, 1999). Additionally, for earthquakes
309 where significant slip is in the high pore pressure zone the average rupture velocities
310 were in the range of 1.2–2.2 km/s (Fig. 7d). This range is comparable to that
311 estimated for tsunami earthquakes (e.g., 2006 Java M_w 7.8 tsunami earthquake which
312 occurred close the Sunda trench and had a rupture velocity range of 1.0 – 1.5 km/s
313 (Ammon et al., 2006)). Hence, the shallow earthquake (blue line in Fig. 4b), with its
314 longer duration, small average stress drop and slow average rupture velocity, appears
315 to be similar to the 1896 Meiji tsunami earthquake (Tanioka and Satake, 1996) (Fig.
316 1).
317
318 ***3.4 Intermediate depth earthquake***
319 For the intermediate earthquake (orange line and dots, Figs 4 and 5),
320 nucleation was in a zone where G^* and G_b^i are large (end of the rock to clay
321 transition), but as rupture propagated up-dip the fault became weaker and G_b^i became
322 smaller in the clay-rich material. Additionally, in thrust environments, seismic waves
323 generated at depth by rupture and reflected back onto the fault by the free surface
324 have been shown to induce tensile normal stress perturbations producing larger stress

drops and slip near the surface (Nielsen, 1998; Oglesby et al., 1998) as well as promoting rupture in shallow velocity-strengthening environments (Kozdon and Dunham, 2013). It has been noted in laboratory experiments where velocity strengthening clays at slow slip-rates and low effective normal stresses (< 30 MPa) become velocity weakening (Saffer and Marone, 2003) and have at the same time low G_b^i at slip-rates comparable to those observed during earthquakes (Faulkner et al., 2011). This means that rupture can easily propagate into clay-rich zones even when there is little initial shear stress present in the accretionary wedge.

This easy rupture propagation in clay-rich zones could explain the large size of 2011 Tohoku earthquake which nucleated at 20 – 25 km depth (Chu et al., 2011). In the case study, rupture travelled up-dip into the wedge, with a significant amount of slip occurring above 15 km depth, which is comparable to the slip inversions for the Tohoku earthquake (e.g. Romano et al., 2014, Fig. 1). The seismic moment release rate from the intermediate asperity is much larger and longer than the deepest and shallowest earthquakes (Fig. 6a) and produced the largest tsunami source (Fig. 6b). In some simulations where the asperity is located at a slightly deeper depth than the intermediate case study, rupture that initially propagates up-dip to the surface then propagated back down the fault again (Fig. 8c), this is a feature that has been suggested for the 2011 M_w 9 earthquake (Ide et al., 2011). Hence, we classify the intermediate simulation as a great thrust earthquake similar to the 2011 M_w 9.0 Tohoku earthquake.

3.5 Deep earthquakes

The relative distance between the asperity and the clay-rich trench is important, this is shown in Fig. 7e where the earthquakes with the largest seismic

moment release had centroid depths between 15 – 20 km. Below a certain depth of ~26 km, the distance from asperity to the clay-rich material was too far relative to the G^* for rupture to reach it; this produced a relatively smaller thrust earthquake (e.g., the 'deep' case study, purple line and dots, in Figs 4-6). These smaller thrust earthquakes had centroid depths below 20 km, had a larger stress drop (Fig. 7b), a faster rupture velocity (Fig. 7d) and larger average G_b^i (Fig. 7f) compared to the great thrust and tsunami earthquakes. They produced only one patch of significant slip making them comparable to the historical M_w 7 – 8 thrust earthquakes in Fig. 1. These historical events appear to be constrained in a depth range of 10 – 40 km and none rupture to the surface despite nucleating at depths relatively shallower than the Tohoku earthquake.

4. Discussion

4.1 Varying scaling between principal stresses

A number of assumptions were made in the construction of the numerical model. In order to determine the robustness of the depth dependent variation of averaged rupture features to variations in some of these assumptions, a sensitivity study was performed on the choice of some of the initial parameters. For example, in the original set of simulations, the principal components of stress were assumed to have a $\sigma_1 = 4.05\,\sigma_3$. In an additional set of 15 simulations, this was changed to $\sigma_1 = 5.0\,\sigma_3$. This was done to evaluate the effect of a different regional principal stresses ratios on the principal findings given that different ratios of 4.7545 (Ma, 2012) and 5.0 (Brace and Kohlstedt, 1980) were used in other studies. Comparing the average moment release, stress drop, G_b^i and rupture velocity per simulation (Fig. S8 in *Supplementary*

375 *Material*), the change in principal stress ratios has not affected the depth dependent
376 features observed in the original set of simulations.
377
378 ***4.2 Varying the fluid retention depth***
379 Another test was done to examine the effect of altering the fluid retention
380 depth, Z_{FRD}. Two additional sets of simulations (15 in each case) were run where z_{FRD}
381 was shifted ± 5 km from the original depth, i.e. 7 km and 17 km. The effect on yield
382 stress and initial stress distributions, can be viewed in the *Supplementary Material*
383 (i.e. Fig. S4 for the original setup, Fig. S6 for Z_{FRD} = 7 km, and Fig. S7 for Z_{FRD} = 17
384 km in Section A5). Fig. 9 shows that the earthquakes in the ensemble with Z_{FRD} = 17
385 km produce more energetic earthquakes (i.e. large moment release and stress drop for
386 intermediate size events). However, the general depth dependent trend observed in
387 the original set of simulations (i.e., Z_{FRD} = 12 km) is still present. This is not the case
388 when Z_{FRD} = 7 km where the depth dependent trends observed in the original study
389 break down with earthquakes at depth exhibiting low rupture velocities (≈ 1 km/s) and
390 long normalised duration. This breakdown in trend is due to the deeper sections of the
391 fault becoming too weak (the yield stress drops below 20 MPa) to store sufficient
392 initial stress relative to the breakdown energy. For Z_{FRD} = 7 km there is still an
393 increase in earthquake moment release at the transition from rock to clay-like material
394 (between 10 - 20 km depth, Fig. 9a) albeit over a reduced scale both in terms of
395 variation in moment and the spatial extent. Therefore, the effect of the rock-clay
396 transition is still present, but as the strength of the deeper section of the fault has
397 become comparable to the near-surface conditions this leads to a breakdown in the
398 original depth-dependent trend. This breakdown in depth-dependent with variation of
399 Z_{FRD} is also applicable to changing the relative difference of the static coefficient of

400 friction between the rock-like and clay-like sections of the fault as it might
401 analogously alter the fault strength.
402
403 ***4.3 Initial stress distributions***
404 The initial stress distributions used in these simulations were based on a single
405 broad asperity model. By lowering the initial stress below the residual shear stress
406 outside of the asperity (i.e., $\tau < \mu_d \sigma_n$) rupture propagation was curtailed. Repeating
407 the case studies presented in Fig. 4 with a higher initial stress outside of the asperity
408 (i.e., $\tau = \mu_d \sigma_n$) produced similar slip distributions for the shallowest and deepest
409 earthquakes (see Fig. 10). The intermediate depth earthquake was larger (with +50 m
410 slip) in comparison with the original simulation. This is due to the intermediate
411 earthquake nucleating near the strongest section of the fault which acts as a barrier in
412 the other two cases. To continue to increase the initial shear stress outside of the
413 asperity would ultimately lead to all earthquakes rupturing the full seismogenic zone
414 with very little constraint on nucleation location and/or initial asperity location.
415 Whether sections of the fault contain shear stress lower than the residual shear
416 strength is unknown; phenomena such as dynamic overshoot and low coupling may
417 contribute to it occurring. Alternative phenomena that would cause rupture arrest
418 include increasing fault strength or G_b^i due to change in effective normal stress (i.e.,
419 due to changes in pore pressure/fault geometry) and/or frictional parameters (i.e.,
420 variations in fault material types). Our simplification provided a method for
421 decoupling rupture features at different depths, and despite its limitations revealed
422 itself effective in clarifying significant general relations between frictional properties
423 and rupture dynamics in a subduction environment.

A less simplistic initial stress distributions could be achieved, for example, by considering multiple asperities of varying sizes on the fault plane. In such a situation rupture becomes more complex, for example rupture velocity and slip-rate have been shown to be strongly affected by sharp changes in initial shear stress and frictional parameters on the fault plane (Huang et al., 2013). In the simulations presented in this study, rupture velocity generally varies smoothly (see Fig. 8) with the exception being in certain cases when the asperity is located at intermediate depths where the rupture jumps to the very high pore pressure zone (Fig. 8c) due to this section of the fault being very weak. This effect could be negated by considering a highly compliant wedge or off-fault an-elastic deformation (as the current numerical model is purely elastic), particularly around the high pore pressure zone, which would slow down the rupture velocity (Lotto et al., 2017; Ma, 2012).

4.4 Along strike variation of frictional parameters

The numerical models presented here are two dimensional and do not account for along strike heterogeneity (i.e. the fault is a line rather than a 2D surface). For example, strong variations in the fluid retention depth along the strike of the fault would lead to along strike variation in fault strength at depth. In our simulations moving the fluid retention depth up 7 km weakened the fault at depth with the result that great earthquakes were no longer generated at depth (compare blue and black dots in Fig. 9). As demonstrated by the smaller size of earthquakes that nucleated at shallow depths in our ensemble of simulations, it is difficult for rupture to propagate into stronger patches of the fault. Shao et al. (2011) proposed that the repeat M7 earthquakes (i.e., 1981 and 2011) occur in relatively weak sections of the fault compared to a potential stronger patch where the 2011 M9 earthquake nucleated. This

449 hypothesis is complementary to our findings whereby along strike variations in the
450 fluid retention depth provides one possible mechanism to explain variations in
451 strength. Other mechanisms such local changes in fault material, fault geometry and
452 pore pressure are other potential means of causing along strike variations in fault
453 strength. On a two-dimensional surface this additional complexity in turn makes
454 rupture propagation more complex as it can conceivably go around barriers while the
455 relative location of surrounding high stress asperities to nucleation can produce
456 rupture directivity (Murphy and Nielsen, 2009).
457
458 ***4.5 Friction Law***
459 Additionally, with the choice of slip weakening friction law, earthquake
460 rupture was generally crack-like in the simulations (Fig. 8). Friction laws where fault
461 strength evolves with slip rate (Dieterich, 1979; Nielsen et al., 2010; Ruina, 1983) are
462 more likely to produce pulse-like ruptures (Nielsen and Carlson, 2000), with shorter
463 rise-time compared to crack-like ruptures. Additionally, velocity-strengthening zones
464 near the surface can further complicate rupture dynamics (Kozdon and Dunham,
465 2013; Lotto et al., 2017). Consequently, it would be beneficial to perform studies with
466 rate-based friction laws in the future.
467 Ultimately, the aim is to simulate the full seismic cycle with friction laws
468 derived from experiments (and physical fault processes) that are consistent with
469 conditions on the fault during the different stages of the seismic cycle. Nevertheless,
470 despite the simplified framework provided by the single asperity model used here, our
471 model manages to reproduce observed geophysical features between the different
472 subduction zone earthquake types in this mega-thrust environment. The observed
473 differences, can, to first order, be ascribed to rupture dynamics effects coupled with a

depth-dependent friction law based that accounts for the expected geology at the Japan Trench.

4.6 Site specific nature of study

Finally, these findings are regional as they are specific to the Tohoku trench environment. A meaningful extrapolation of these results to other subduction zones would require at least similarity in depth dependent frictional properties and fault geometry. For example, in this study, frictional properties based on a clay-like material was chosen as this was observed at Tohoku (Chester et al., 2013). However, soft sediment in the nearby Nankai trench is more sandy in nature (Hirono et al., 2014). Dynamic simulations comparing the two environments have shown that a more sandy sediment produces a larger thermal pressurisation during dynamic rupture but this is offset by higher initial excess fluid pressure (Hirono et al., 2016). Consequently, care must be taken in applying the finds from one subduction zone to another.

5. Conclusion

In nature, subduction zone faults are more complicated than what is depicted in our numerical models (fault roughness, multiple asperities, off-fault an-elastic deformation etc.). Nevertheless, our model based on lithological and depth dependent friction law tuned to the 2011 Tohoku fault region allows us to better understand and reproduce to the first order the different types of tsunamigenic earthquakes. Consistently with geophysical observations, our models have shown that events with a number of characteristics resembling tsunami earthquakes were generated in the accretionary wedge. Their rupture area was constrained to remain there due to the

fault strength and breakdown energy increasing with depth. We also found that standard thrust earthquakes, with relatively larger stress drops, shorter durations and faster rupture velocities occurred in crystalline rock where both the energy release rate and fault resistance are high. Finally, if the rupture initiated at the bottom of or just below the rock-clay transition and propagated towards the surface, the drop in fault strength and frictional resistance lead to the production of great thrust earthquakes.

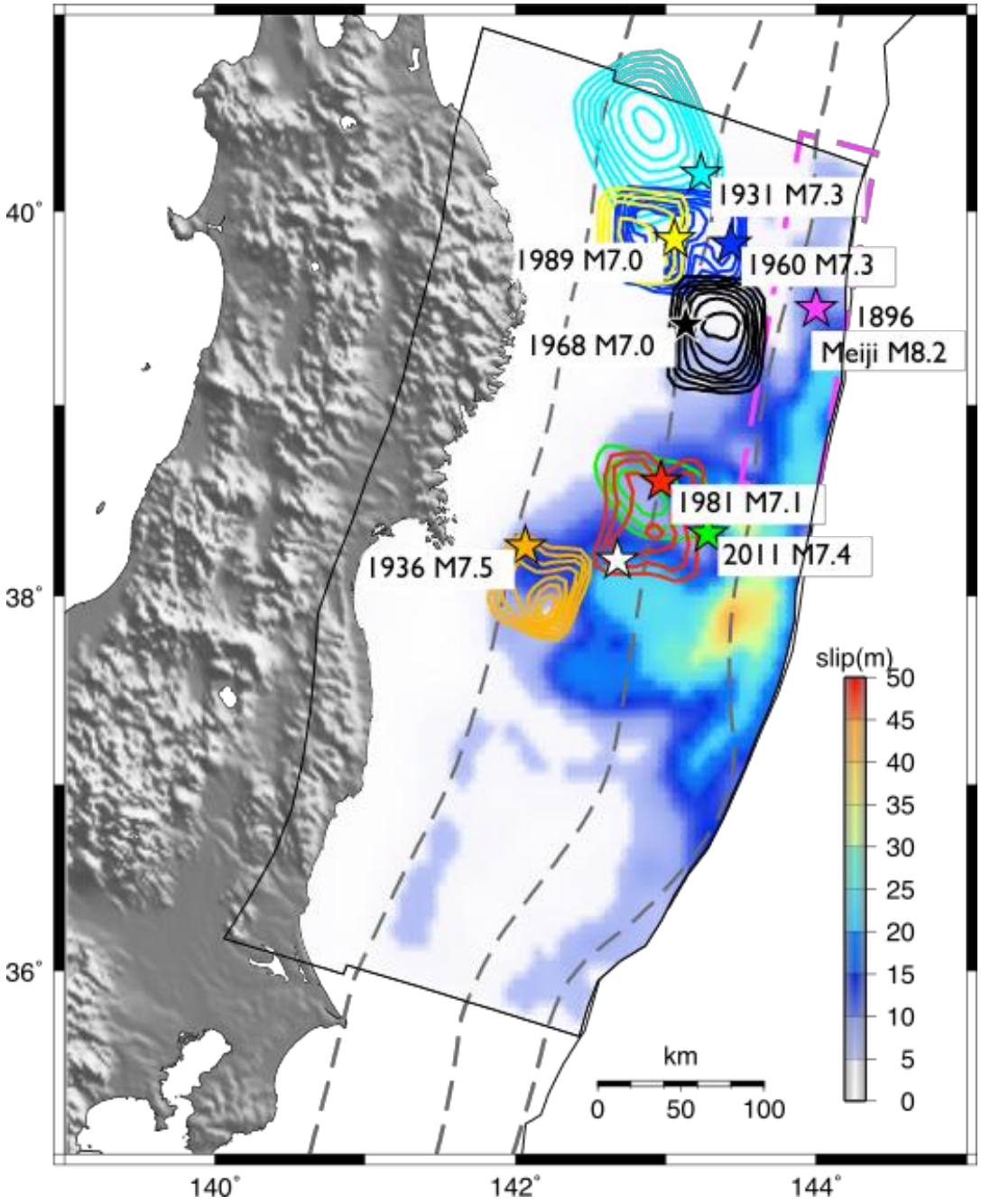

509

510 **Figure 1**: Earthquake history off the Pacific coast of Tohoku region and model setup.

511 Coloured contours represent slip distributions at 0.5 m interval for a number of

512 historical thrust earthquakes(Shao et al., 2011; Yamanaka and Kikuchi, 2004); The

513 magenta dashed box represents the location for the 1896 Meiji tsunami earthquakes

514 (M 8.2-8.4). The colour slip distribution is the M_w 9 Tohoku earthquake(Romano et

515 al., 2014), the red star is its epicentre. Dashed grey line is depth at 10, 20 and 40 km.

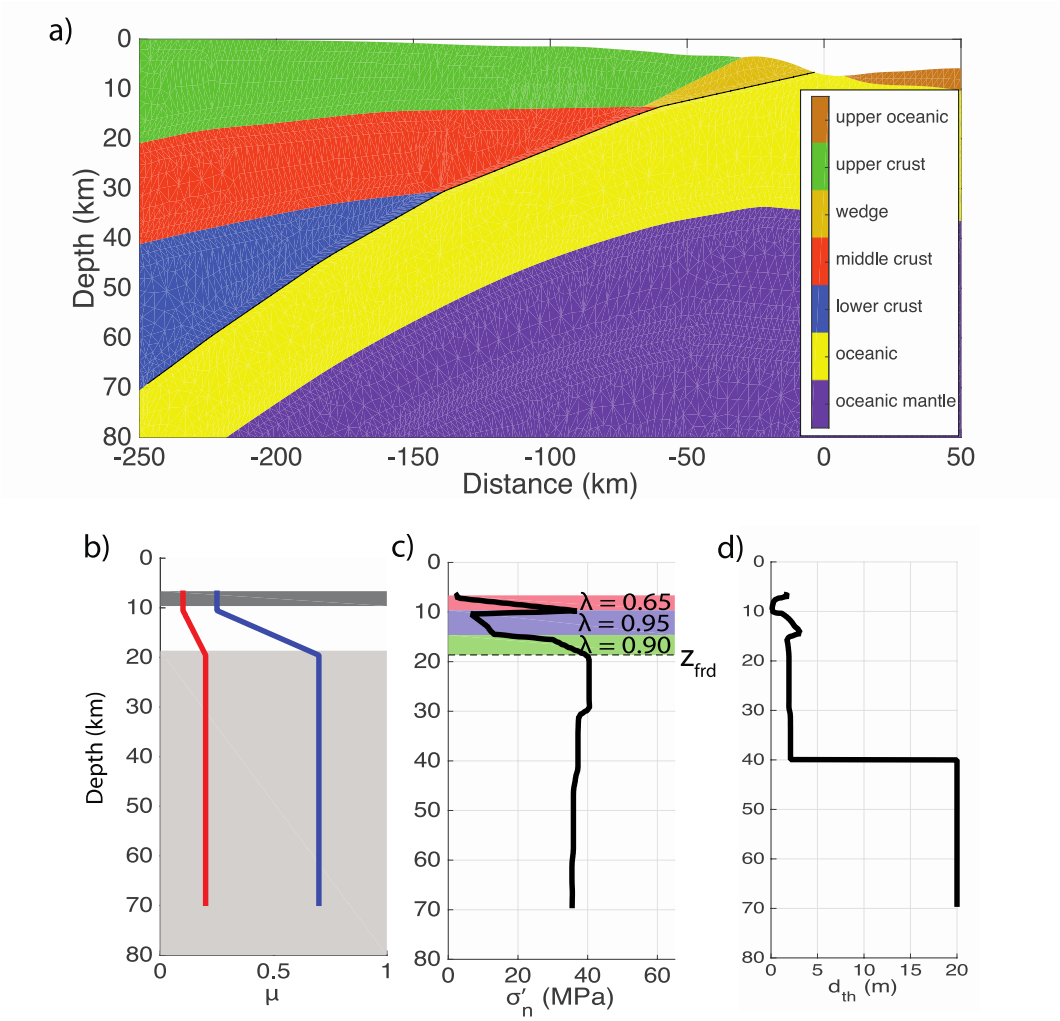

Figure 2: Numerical model set up. **a)** structural model used in the numerical simulations, black line denotes the subduction interface. **b)** variation of frictional coefficients with depth: the dark and light grey boxes denote the clay-rich and crystalline rock frictional coefficients; the white is the transition between the two materials. Solid blue and red lines are the static and dynamic coseismic coefficients of friction respectively. **c)** the variation of the effective normal stress with depth, coloured boxes denote different pore fluid to overburden stress ratio, λ. The dashed

black line denotes the fluid retention depth. **d)** variance of d_{th} with depth which is a function of effective normal stress and frictional material type (i.e., rock or clay-rich).

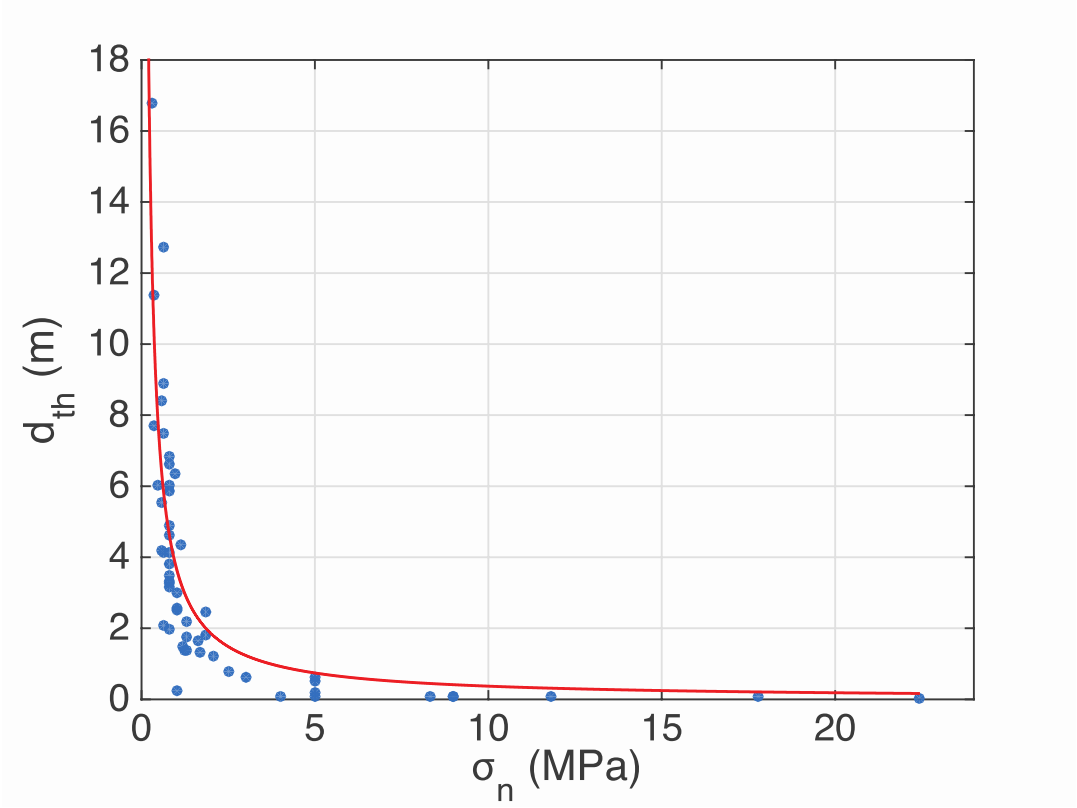

Figure 3: The fit of $d_{th} = 3.712\ \|\sigma_n\|^{-1}$ (red line) compared with the laboratory experiments performed on clay material (see Table S5 in *Supplementary Material* for references).

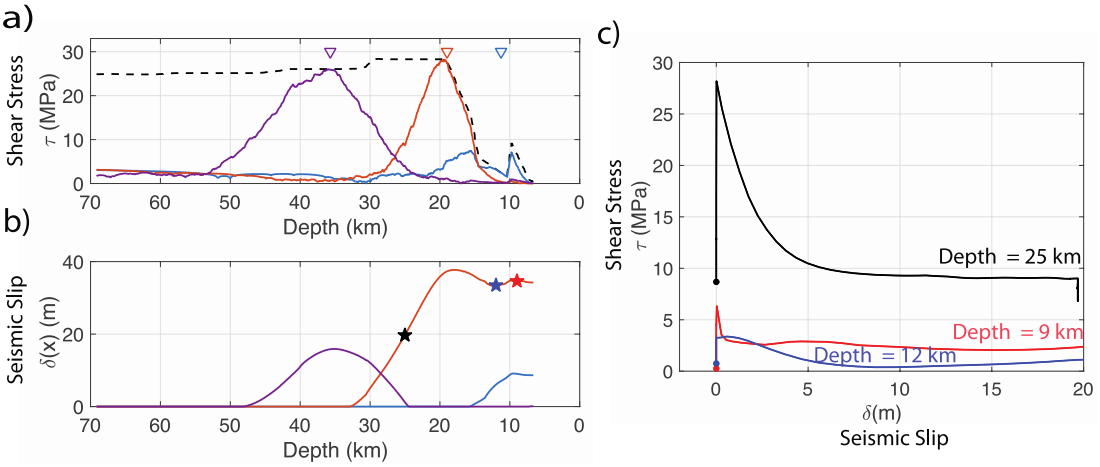

536

537 **Figure 4:** Modelled environment earthquake source parameters **a)** The different solid
538 colours relate to the initial shear stress distributions used in the three simulations
539 which reproduce a tsunamigenic great thrust earthquake (orange), tsunami earthquake
540 (blue) and thrust earthquakes (purple). The same colour code is used for all subplots.
541 Triangles are nucleation locations. Black dashed line is the fault strength. **b)** Slip
542 distributions resulting from simulations where the colours relate to the initial stress
543 distributions in a). **c)** Shear stress evolution with slip at three different depths (25 km
544 black line, 12 km blue line, 9 km red line) taken from intermediate simulation (i.e.,
545 orange line in b). The locations are also highlighted by stars in subplot b) where a
546 similar colour scale has been used. Dots denote the initial stress at each location.

547

548

549

550

551

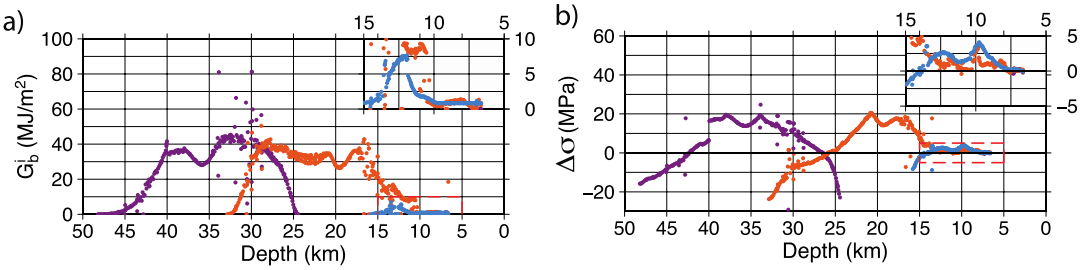

552

553 **Figure 5: a)** Breakdown energy calculated at each point along the fault. Insets are

554 expansions of the data inside the red dashed boxes. **b)** Static stress drop calculated at

555 each point along the fault.

556

557

558

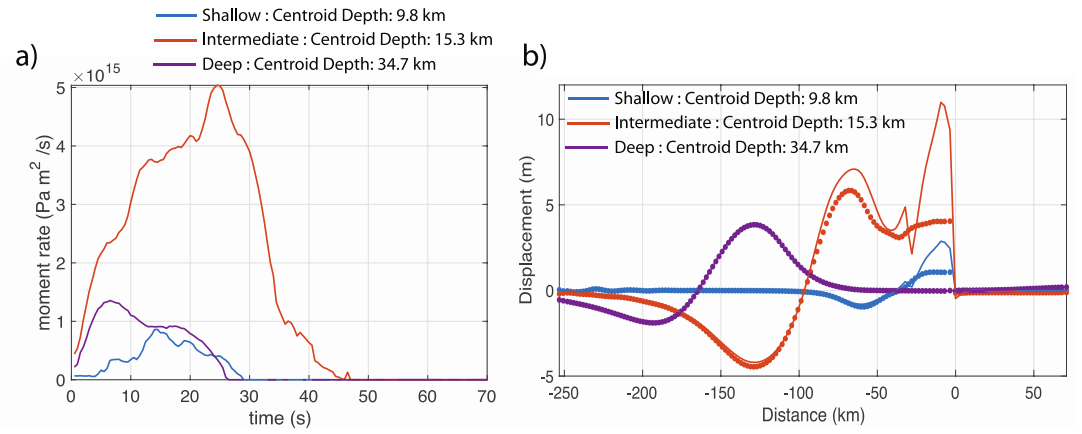

559

560 **Figure 6: a)** Moment release rate with time. **b)** Vertical seafloor displacement (dotted

561 lines) and estimated tsunami source (solid lines, details in Section A3 in

562 *Supplementary Information*). Horizontal distance as in Fig. 2 where 0 km indicates the

563 point where the fault reaches the seafloor.

564

565

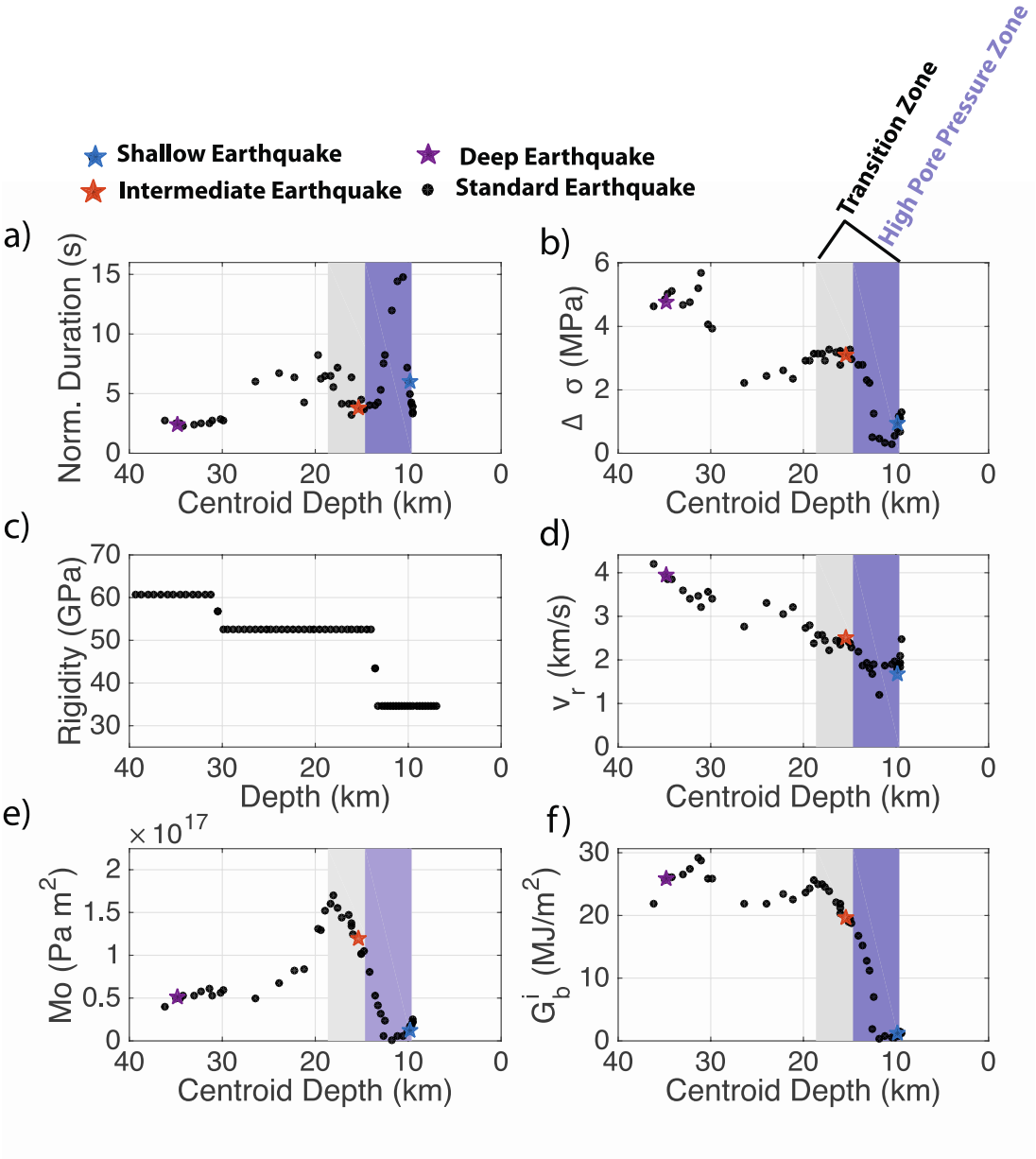

566

567 **Figure 7:** Rupture parameters plotted against centroid depth for a number of
568 simulations where only the location of the high stress asperity varies with depth. The
569 purple box is the zone with very high pore pressure ($\lambda = 0.95$); grey and purple boxes
570 together demark the transition zone between clay-like and crystalline rock frictional
571 parameters. **a)** Normalised earthquake duration; **b)** Average static stress drop; **c)** shear
572 modulus averaged across the fault plane to account of bi-material wall rocks; **d)**
573 Average rupture velocity; **e)** Moment of the (1D) simulated earthquakes (details in

574 Section A4 in *Supplementary Material*); and **f)** Average breakdown energy. The stars
575 indicate the three case studies presented in Fig. 2 with the same colour code applied.
576
577
578

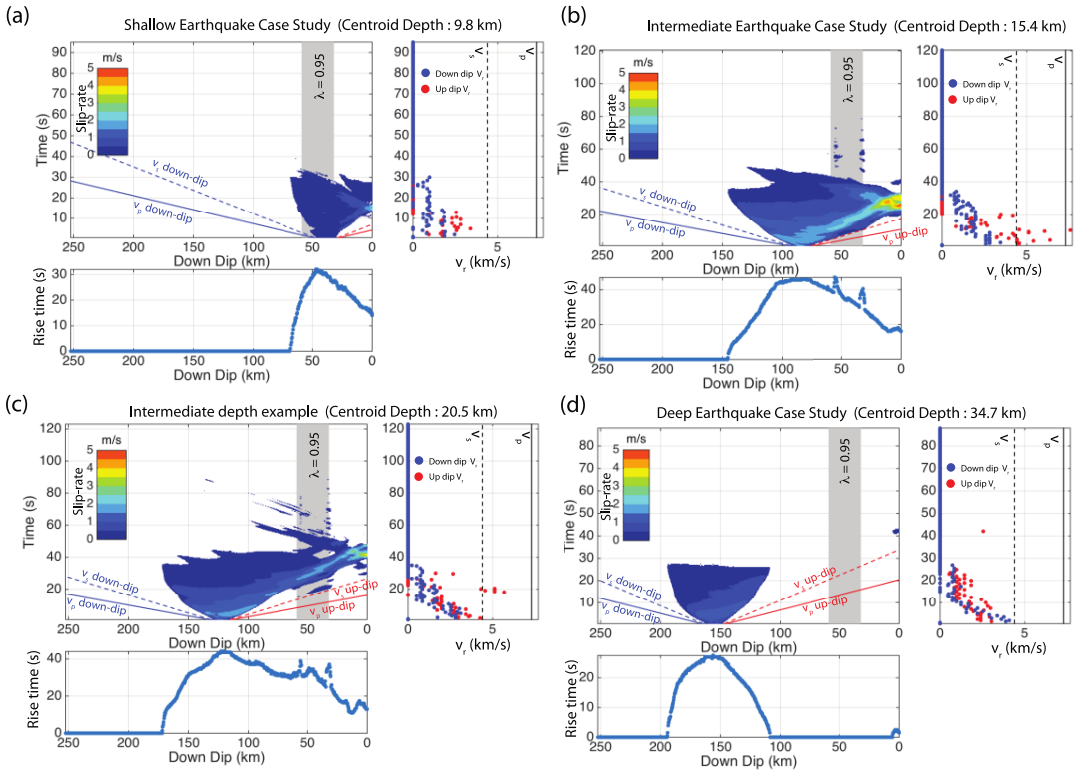

579

580 **Figure 8**: Slip-rate, rupture velocity and rise-time observed in four simulations with
581 increasing fault down-dip location of the asperity (40, 80, 120 and 160 km depth,
582 respectively). These depths correspond to the hypocentral depths of the three cases
583 presented in Fig. 2 and an additional great thrust earthquake which generated a down-
584 dip travelling rupture pulse. In all subplots the solid and dashed lines are the P- and S-
585 wave velocities in the oceanic material (i.e., yellow layer in Fig. 1) with the colour of
586 the line indicating rupture direction (i.e. blue is to the left of the nucleation zone or
587 down-dip, red is the right or up-dip). The light grey box behind the slip-rates defines
588 the zone of very high pore pressure (i.e., $\lambda = 0.95$) in the wedge. **a)** Asperity in the

wedge which corresponds to the shallow case study (blue line and dots in Figs. 2 and 3) **b)** Asperity at 20 km depth related to the intermediate case study (i.e., orange data in Figs. 2 and 3). **c)** Asperity at 27 km depth, an example of a great thrust earthquake with a down-dip travelling rupture pulse that was referred to in Section 3.4 **d)** Deep case study (i.e., 39 km) purple colour in Figs. 2 and 3.

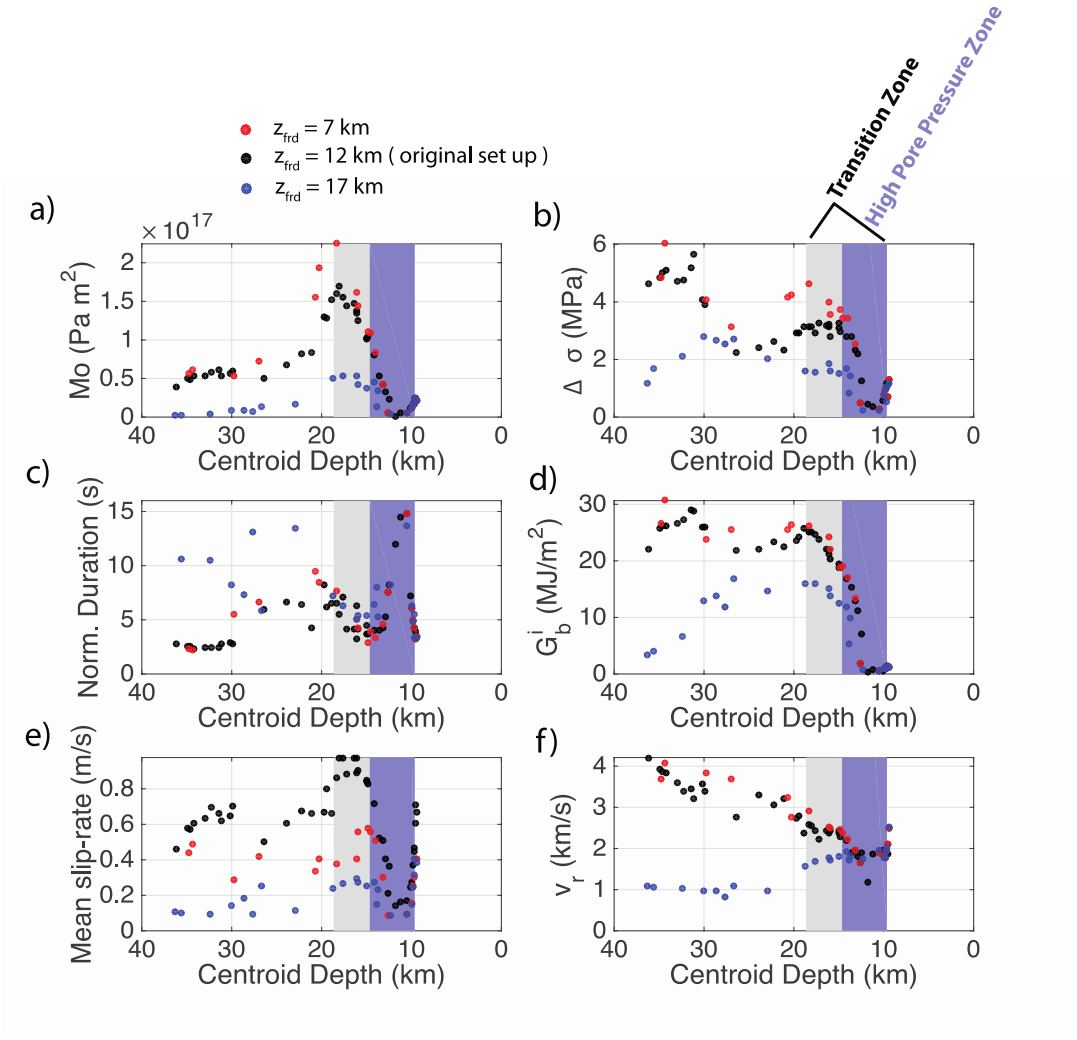

Figure 9: Sensitivity study on varying the fluid retention depth. The black dots are from simulations using the original model discussed in Section 3 (i.e., z_{FRD} = 12 km)

600 with 45 simulations, the blue dots are the case z_{FRD} = 7 km (15 simulations) and the
601 red dots are case with z_{FRD} = 17 km (15 simulations). **a)** Seismic moment of the
602 simulated earthquake; a constant shear modulus G = 30 GPa rather than a depth
603 dependent shear modulus was used in the calculation as it is commonly used in
604 observational seismology, **b)** Average static stress drop, **c)** average normalised rupture
605 duration, **d)** average breakdown energy, **e)** average slip-rate per earthquake and **f)**
606 average rupture velocity.
607

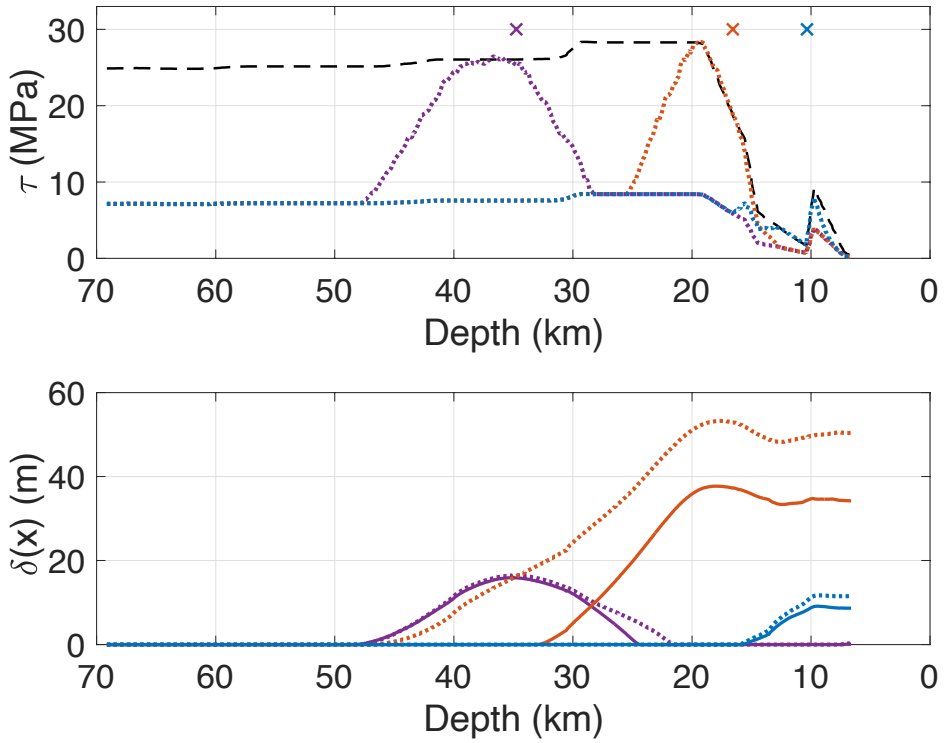

608

609 **Figure 10:** Testing increased background initial stress outside of the asperity. **a)** The
610 black dashed line is the yield strength. The dotted colour lines represent the initial
611 shear stress where stress does not drop below the residual shear stress (i.e. $\tau = \mu_d \sigma_n$).
612 The x's are the nucleation locations for the new (i.e. dashed) set of simulations. **b)** the
613 final slip distributions for each simulation where the colour and line type convention

is same as the one used in subplot a) The solid lines are the slip distributions using the original initial stress distribution (see Fig. 4).

References

Abercrombie, R., Rice, J., 2005. Can observations of earthquakes scaling constrain slip weakening. Geophys. J. Int. 162, 406–424. doi:10.1111/j.1365-246X.2005.02579.x

Ammon, C.J., Kanamori, H., Lay, T., Velasco, A.A., 2006. The 17 July 2006 Java tsunami earthquake. Geophys. Res. Lett 33, L24308–5. doi:10.1029/2006GL028005

Bilek, S.L., Lay, T., 1999. Rigidity variations with depth along interplate megathrust faults in subduction zones. Nature 400, 443–446. doi:10.1038/22739

Bilek, S.L., Rotman, H.M.M., Phillips, W.S., 2016. Low stress drop earthquakes in the rupture zone of the 1992 Nicaragua tsunami earthquake. Geophys. Res. Lett 43, 10,180–10,188. doi:10.1002/2016GL070409

Brace, W.F., Kohlstedt, D.L., 1980. Limits on lithospheric stress imposed by laboratory experiments. J. Geophys. Res. 85, 6248–6252. doi:10.1029/JB085iB11p06248

Chester, F.M., Rowe, C., Ujiie, K., Kirkpatrick, J., Regalla, C., Remitti, F., Moore, J.C., Toy, V., Wolfson-Schwehr, M., Bose, S., Kameda, J., Mori, J.J., Brodsky, E.E., Eguchi, N., Toczko, S., Expedition 343 and 343T Scientists, 2013. Structure and Composition of the Plate-Boundary Slip Zone for the 2011 Tohoku-Oki Earthquake. Science 342, 1208–1211. doi:10.1126/science.1243719

Chu, R., Wei, S., Helmberger, D.V., Zhan, Z., Zhu, L., Kanamori, H., 2011. Initiation of the great Mw 9.0 Tohoku–Oki earthquake. Earth Planet. Sci. Lett. 308, 277–283. doi:10.1016/j.epsl.2011.06.031

Cochard, A., Madariaga, R., 1996. Complexity of seismicity due to highly rate-dependent friction. J. Geophys. Res. 101, 25,321–25,336.

Cubas, N., Lapusta, N., Avouac, J.-P., Perfettini, H., 2015. Numerical modeling of long-term earthquake sequences on the NE Japan megathrust: Comparison with observations and implications for fault friction. Earth Planet. Sci. Lett. 419, 187–198. doi:10.1016/j.epsl.2015.03.002

Del Gaudio, P., Di Toro, G., Han, R., Hirose, T., Nielsen, S., Shimamoto, T., Cavallo, A., 2009. Frictional melting of peridotite and seismic slip. J. Geophys. Res. 114, B06306–19. doi:10.1029/2008JB005990

Di Toro, G., Han, R., Hirose, T., De Paola, N., Nielsen, S., Mizoguchi, K., Ferri, F., Cocco, M., Shimamoto, T., 2011. Fault lubrication during earthquakes. Nature 471, 494–498. doi:10.1038/nature09838

Dieterich, J., 1979. Modeling of Rock Friciton: 1. Experimental results and constituive equations. J. Geophys. Res. 84, 2161–2168.

Faulkner, D.R., Mitchell, T.M., Behnsen, J., Hirose, T., Shimamoto, T., 2011. Stuck in the mud? Earthquake nucleation and propagation through accretionary forearcs. Geophys. Res. Lett 38. doi:10.1029/2011GL048552

Festa, G., Vilotte, J.-P., 2005. The Newmark scheme as velocity–stress time-

staggering: an efficient PML implementation for spectral element simulations of elastodynamics. Geophys. J. Int. 161, 789–812. doi:10.1111/j.1365-246X.2005.02601.x

Freed, A., 2005. Earthquake triggering by static, dynamic, and postseismic stress transfer. Annu. Rev. Earth Planet Sci. 33, 335–367. doi:http://dx.doi.org/10.1146/annurev.earth.33.092203.122505

Gao, X., Wang, K., 2014. Strength of stick-slip and creeping subduction megathrusts from heat flow observations. Science 345, 1038–1041. doi:10.1126/science.1255487

Geist, E.L., Bilek, S.L., 2001. Effect of depth-dependent shear modulus on tsunami generation along subduction zones. Geophys. Res. Lett 28, 1315–1318. doi:10.1029/2000GL012385

Hacker, B.R., Abers, G.A., Peacock, S.M., 2003a. Subduction factory 1. Theoretical mineralogy, densities, seismic wave speeds, and H2O contents. J Geophys Res 108, 1–26. doi:10.1029/2001JB001127

Hacker, B.R., Peacock, S.M., Abers, G.A., Holloway, S.D., 2003b. Subduction factory 2. Are intermediate-depth earthquakes in subducting slabs linked to metamorphic dehydration reactions? J. Geophys. Res. 108, 1–20. doi:10.1029/2001JB001129

Hartog, den, S.A.M., Niemeijer, A.R., Spiers, C.J., 2012. New constraints on megathrust slip stability under subduction zone P–T conditions. Earth and Planetary Science Letters 353-354, 240–252. doi:10.1016/j.epsl.2012.08.022

Hayes, G.P., Wald, D.J., Johnson, R.L., 2012. Slab1.0: A three-dimensional model of global subduction zone geometries. J. Geophys. Res. 117, B01302–15. doi:10.1029/2011JB008524

Hirono, T., Ishikawa, T., Masumoto, H., Kameda, J., Yabuta, H., Mukoyoshi, H., 2014. Re-evaluation of frictional heat recorded in the dark gouge of the shallow part of a megasplay fault at the Nankai Trough. Tectonophysics 626, 157–169. doi:10.1016/j.tecto.2014.04.020

Hirono, T., Tsuda, K., Tanikawa, W., Ampuero, J.-P., Shibazaki, B., Kinoshita, M., Mori, J.J., 2016. Near-trench slip potential of megaquakes evaluated from fault properties and conditions. Sci. Rep. 1–13. doi:10.1038/srep28184

Huang, Y., Ampuero, J.-P., Kanamori, H., 2013. Slip-Weakening Models of the 2011 Tohoku-Oki Earthquake and Constraints on Stress Drop and Fracture Energy. Pure Appl. Geophys. 171, 2555–2568. doi:10.1007/s00024-013-0718-2

Hyndman, R., Yamano, M., Oleskevich, D., 1997. The seismogenic zone of subduction thrust faults. The Island Arc 6, 244–260.

Ida, Y., 1972. Cohesive Force across the Tip of a Longitudinal-Shear Crack and Griffith's Specific Surface Energy. J. Geophys. Res. 77, 3796–3805.

Ide, S., Baltay, A., Beroza, G.C., 2011. Shallow Dynamic Overshoot and Energetic Deep Rupture in the 2011 Mw 9.0 Tohoku-Oki Earthquake. Science 332, 1426–1429. doi:10.1126/science.1207020

Ihmlé, P.F., 1996. Monte Carlo slip inversion in the frequency domain:: Application to the 1992 Nicaragua Slow Earthquake. Geophys. Res. Lett 23, 913–916. doi:10.1029/96GL00872

Ikari, M.J., Saffer, D.M., Marone, C., 2007. Effect of hydration state on the frictional properties of montmorillonite-based fault gouge. J. Geophys. Res. 112, B06423–12. doi:10.1029/2006JB004748

Kanamori, H., 1972. Mechanism of tsunami earthquakes. Phys. Earth Planet. In. 6, 346–359. doi:10.1016/0031-9201(72)90058-1

709 Kato, N., 2012. Dependence of earthquake stress drop on critical slip-weakening
710 distance. J Geophys Res 117. doi:10.1029/2011JB008359
711 Kimura, G., Hina, S., Hamada, Y., Kameda, J., Tsuji, T., Kinoshita, M., Yamaguchi,
712 A., 2012. Runaway slip to the trench due to rupture of highly pressurized
713 megathrust beneath the middle trench slope: The tsunamigenesis of the 2011
714 Tohoku earthquake off the east coast of northern Japan. Earth Planet. Sci. Lett.
715 339-340, 32–45. doi:10.1016/j.epsl.2012.04.002
716 Kozdon, J.E., Dunham, E.M., 2014. Constraining shallow slip and tsunami excitation
717 in megathrust ruptures using seismic and ocean acoustic waves recorded on
718 ocean-bottom sensor networks. Earth Planet. Sci. Lett. 396, 56–65.
719 doi:10.1016/j.epsl.2014.04.001
720 Kozdon, J.E., Dunham, E.M., 2013. Rupture to the Trench: Dynamic Rupture
721 Simulations of the 11 March 2011 Tohoku Earthquake. B. Seismol. Soc. Am.
722 103, 1275–1289. doi:10.1785/0120120136
723 Lay, T., Kanamori, H., Ammon, C.J., Koper, K.D., Hutko, A.R., Ye, L., Yue, H.,
724 Rushing, T.M., 2012. Depth-varying rupture properties of subduction zone
725 megathrust faults. J. Geophys. Res. 117, B04311–21. doi:10.1029/2011JB009133
726 Lotto, G.C., Dunham, E.M., Jeppson, T.N., Tobin, H.J., 2017. The effect of compliant
727 prisms on subduction zone earthquakes and tsunamis. Earth Planet. Sci. Lett. 458,
728 213–222. doi:10.1016/j.epsl.2016.10.050
729 Ma, S., 2012. A self-consistent mechanism for slow dynamic deformation and
730 tsunami generation for earthquakes in the shallow subduction zone. Geophys.
731 Res. Lett 39, n/a–n/a. doi:10.1029/2012GL051854
732 Meneghini, F., Di Toro, G., Rowe, C.D., Moore, J.C., Tsutsumi, A., Yamaguchi, A.,
733 2010. Record of mega-earthquakes in subduction thrusts: The black fault rocks of
734 Pasagshak Point (Kodiak Island, Alaska). Geol. Soc. Am. Bull. 122, 1280–1297.
735 doi:10.1130/B30049.1
736 Mitsui, Y., Yagi, Y., 2013. An interpretation of tsunami earthquake based on a simple
737 dynamic model: Failure of shallow megathrust earthquake. Geophys. Res. Lett
738 40, 1523–1527. doi:10.1002/grl.50266
739 Miura, S., Takahashi, N., Nakanishi, A., Tsuru, T., Kodaira, S., Kaneda, Y., 2005.
740 Structural characteristics off Miyagi forearc region, the Japan Trench seismogenic
741 zone, deduced from a wide-angle reflection and refraction study. Tectonophysics
742 407, 165–188. doi:10.1016/j.tecto.2005.08.001
743 Murphy, S., Nielsen, S., 2009. Estimating earthquake magnitude with early arrivals: A
744 test using dynamic and kinematic models. B. Seismol. Soc. Am. 99, No. 1, 1–23.
745 doi:http://dx.doi.org/10.1785/0120070246
746 Murphy, S., Scala, A., Herrero, A., Lorito, S., Festa, G., Trasatti, E., Tonini, R.,
747 Romano, F., Molinari, I., Nielsen, S., 2016. Shallow slip amplification and
748 enhanced tsunami hazard unravelled by dynamic simulations of mega-thrust
749 earthquakes. Sci. Rep. 1–12. doi:10.1038/srep35007
750 Nalbant, S., McCloskey, J., Steacy, S., NicBhloscaidh, M., Murphy, S., 2013.
751 Interseismic coupling, stress evolution, and earthquake slip on the Sunda
752 megathrust. Geophys. Res. Lett 40, 4204–4208. doi:10.1002/grl.50776
753 Nielsen, S., Carlson, J., 2000. Rupture Pulse Characterization: Self-Healing, Self-
754 Similar, Expanding Solutions in a Continuum Model of Fault Dynamic. B.
755 Seismol. Soc. Am. 90, No. 6, 1480–1497.
756 Nielsen, S., Mosca, P., Giberti, G., Di Toro, G., Hirose, T., Shimamoto, T., 2010. On
757 the transient behavior of frictional melt during seismic slip. J. Geophys. Res. 115,
758 B10301–17. doi:10.1029/2009JB007020

759 Nielsen, S., Spagnuolo, E., Violay, M., Smith, S., Toro, G., Bistacchi, A., 2016. G:
760 Fracture energy, friction and dissipation in earthquakes. J. Seismol. 1–19.
761 doi:10.1007/s10950-016-9560-1
762 Nielsen, S.B., 1998. Free surface effects on the propagation of dynamic rupture.
763 Geophys. Res. Lett. 25, 125–128.
764 Niemeijer, A., Di Toro, G., Nielsen, S., Di Felice, F., 2011. Frictional melting of
765 gabbro under extreme experimental conditions of normal stress, acceleration, and
766 sliding velocity. J. Geophys. Res. 116. doi:10.1029/2010JB008181
767 Noda, H., Lapusta, N., 2013. Stable creeping fault segments can become destructive
768 as a result of dynamic weakening. Nature 493, 518–521. doi:10.1038/nature11703
769 Oglesby, D., Archuleta, R., Nielsen, S., 1998. Earthquakes on Dipping Faults: The
770 Effects of Broken Symmetry. Science 280, 1055–1059.
771 doi:http://dx.doi.org/10.1126/science.280.5366.1055
772 Ozawa, S., Nishimura, T., Suito, H., Kobayashi, T., Tobita, M., Imakiire, T., 2011.
773 Coseismic and postseismic slip of the 2011 magnitude-9 Tohoku-Oki earthquake.
774 Nature 475, 373–376. doi:10.1038/nature10227
775 Proctor, B.P., Mitchell, T.M., Hirth, G., Goldsby, D., Zorzi, F., Platt, J.D., Di Toro,
776 G., 2014. Dynamic weakening of serpentinite gouges and bare surfaces at seismic
777 slip rates. J. Geophys. Res. 119, 8107–8131. doi:10.1002/2014JB011057
778 Remitti, F., Smith, S.A.F., Mittempergher, S., Gualtieri, A.F., Di Toro, G., 2015.
779 Frictional properties of fault zone gouges from the J-FAST drilling project (M
780 w9.0 2011 Tohoku-Oki earthquake). Geophys. Res. Lett 42, 2691–2699.
781 doi:10.1002/2015GL063507
782 Romano, F., Trasatti, E., Lorito, S., Piromallo, C., Piatanesi, A., Ito, Y., Zhao, D.,
783 Hirata, K., Lanucara, P., Cocco, M., 2014. Structural control on the Tohoku
784 earthquake rupture process investigated by 3D FEM, tsunami and geodetic data.
785 Sci. Rep. 4. doi:10.1038/srep05631
786 Rubin, A.M., Ampuero, J.-P., 2007. Aftershock asymmetry on a bimaterial interface.
787 Journal of Geophysical Research 112, B05307–23. doi:10.1029/2006JB004337
788 Ruina, A., 1983. Slip instablity and state variable friction law. J. Geophys. Res. 88,
789 10359–10370.
790 Saffer, D.M., Lockner, D.A., McKiernan, A., 2012. Effects of smectite to illite
791 transformation on the frictional strength and sliding stability of intact marine
792 mudstones. Geophys. Res. Lett. 39, L11304. doi:10.1029/2012GL051761
793 Saffer, D.M., Marone, C., 2003. Comparison of smectite- and illite-rich gouge
794 frictional properties: application to the updip limit of the seismogenic zone along
795 subduction megathrusts. Earth Planet. Sci. Lett. 215, 219–235.
796 doi:10.1016/S0012-821X(03)00424-2
797 Satake, K., Tanioka, Y., 1999. Sources of Tsunami and Tsunamigenic Earthquakes in
798 Subduction Zones, in: Seismogenic and Tsunamigenic Processes in Shallow
799 Subduction Zones. Pure Appl. Geophys. 154, 467–483. doi:10.1007/978-3-0348-
800 8679-6_5
801 Sawai, M., Hirose, T., Kameda, J., 2014. Frictional properties of incoming pelagic
802 sediments at the Japan Trench: implications for large slip at a shallow plate
803 boundary during the 2011 Tohoku earthquake. Earth, Planets Space 66, 65.
804 doi:10.1186/1880-5981-66-65
805 Scala, A., Festa, G., Vilotte, J.-P., 2017. Rupture dynamics along bimaterial
806 interfaces: a parametric study of the shear-normal traction coupling. Geophys. J.
807 Int. 209, 1. doi:10.1093/gji/ggw489
808 Shao, G., Ji, C., Zhao, D., 2011. Rupture process of the 9 March, 2011 Mw 7.4

Sanriku-Oki, Japan earthquake constrained by jointly inverting teleseismic waveforms, strong motion data and GPS observations. Geophys. Res. Lett. 38, L00G20. doi:10.1029/2011GL049164

Shibazaki, B., Matsuzawa, T., Tsutsumi, A., 2011. 3D modeling of the cycle of a great Tohoku-Oki earthquake, considering frictional behavior at low to high slip velocities. Gephys. Res. Lett. 38, L21305. doi: 10.1029/2011GL049308

Suppe, J., 2014. Fluid overpressures and strength of the sedimentary upper crust. J. Struct. Geol. 69, 481-492. doi:10.1016/j.jsg.2014.07.009

Tanioka, Y., Satake, K., 1996. Fault parameters of the 1896 Sanriku Tsunami Earthquake estimated from Tsunami Numerical Modeling. Geophys. Res. Lett 23, 1549–1552. doi:10.1029/96GL01479

Ujiie, K., Tanaka, H., Saito, T., Tsutsumi, A., Mori, J.J., Kameda, J., Brodsky, E.E., Chester, F.M., Eguchi, N., Toczko, S., Expedition 343 and 343T Scientists, 2013. Low Coseismic Shear Stress on the Tohoku-Oki Megathrust Determined from Laboratory Experiments. Science 342, 1211–1214. doi:10.1126/science.1243485

Violay, M., Di Toro, G., Gibert, B., Nielsen, S., Spagnuolo, E., Del Gaudio, P., Azais, P., Scarlato, P.G., 2014. Effect of glass on the frictional behavior of basalts at seismic slip rates. Geophys. Res. Lett. 41, 348–355. doi:10.1002/ 2013GL058601

Wang, K., Hu, Y., 2006. Accretionary prisms in subduction earthquake cycles: The theory of dynamic Coulomb wedge. J. Geophys. Res. 111, B06410. doi:10.1029/2005JB004094

Wang, K., Hu, Y., Huene, von, R., Kukowski, N., 2010. Interplate earthquakes as a driver of shallow subduction erosion. Geology 38, 431–434. doi:10.1130/G30597.1

Yamanaka, Y., Kikuchi, M., 2004. Asperity map along the subduction zone in northeastern Japan inferred from regional seismic data. J. Geophys. Res. 109, 1–16. doi:10.1029/2003JB002683

Acknowledgements: S.M., G.D.T., E.S., S.N., S.A. were supported by the European Research Council Consolidator Grant Project No. 614705 NOFEAR . S.L. and A.P were supported by the European Union's Seventh Framework Programme (FP7/2007-2013) under grant agreement n° 603839 (Project ASTARTE - Assessment, Strategy and Risk Reduction for Tsunamis in Europe). All of the figures have been created using either MATLAB (www.mathworks.com) and Generic Mapping Tools (http://gmt.soest.hawaii.edu). Two anonymous reviewers and the Editor are acknowledged for their constructive comments which further improved the paper.

Author Contributions: S.M. performed the numerical simulations. G.D.T., E.S., S.A. and S.N. provided frictional parameters for numerical models from both experiments they performed and literature. F.R. digitised slip distributions from historical earthquakes. Tsunami source estimates provided by F.R. and A.S.; G.F. and A.S. developed the numerical code. Concept development: S.M., G.D.T., S.L. and E.S; important ideas provided by S.N., G.F. and A.P. throughout the development of the work. All authors contributed to text and revised the manuscript several times.

Additional Information

The authors declare no competing financial interests. Correspondence and requests for materials should be addressed to S.M. (shane.murphy@ifremer.fr).

Figure 1
Click here to download Figure: fig1.eps

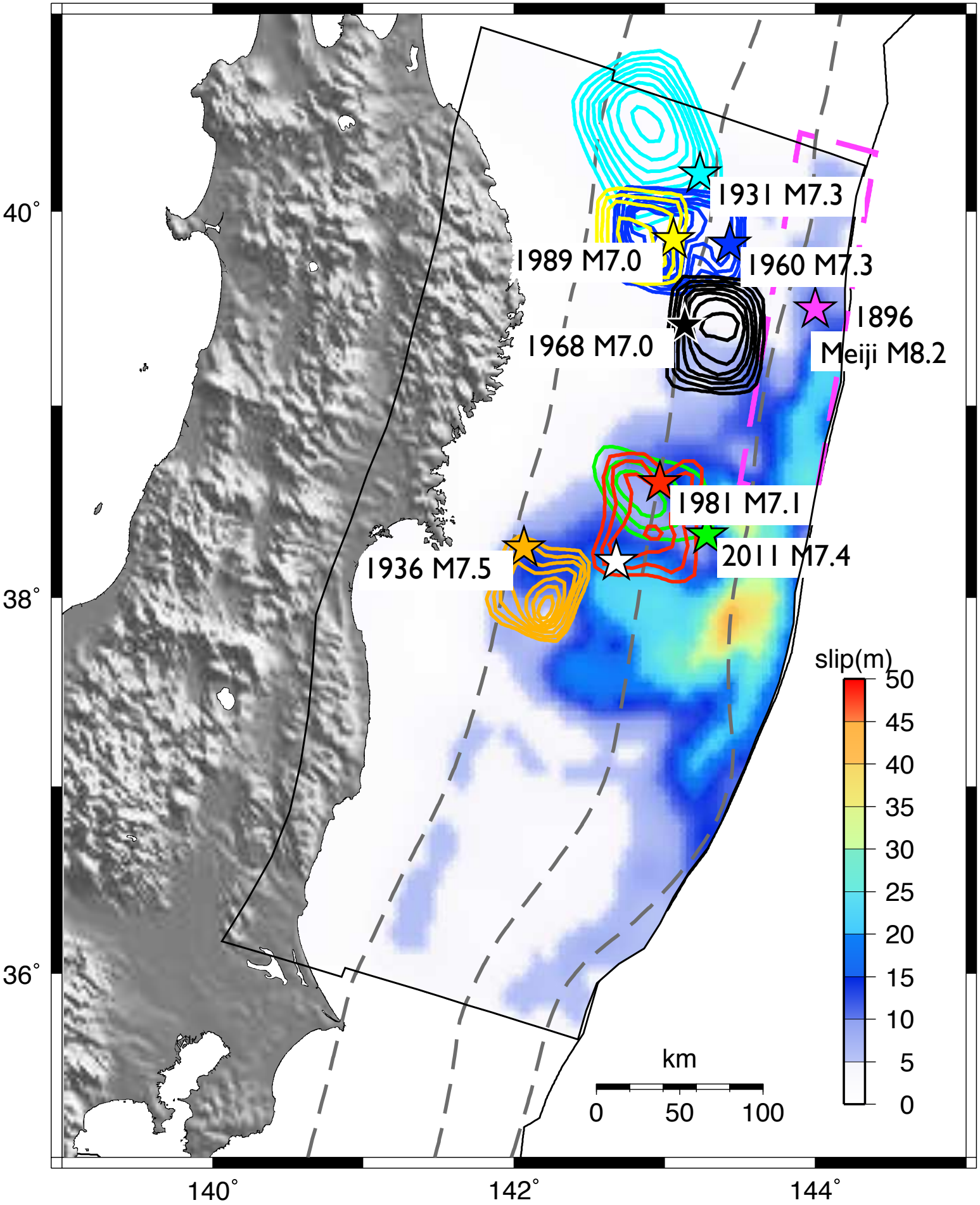

Figure 2
Click here to download Figure: fig2.pdf

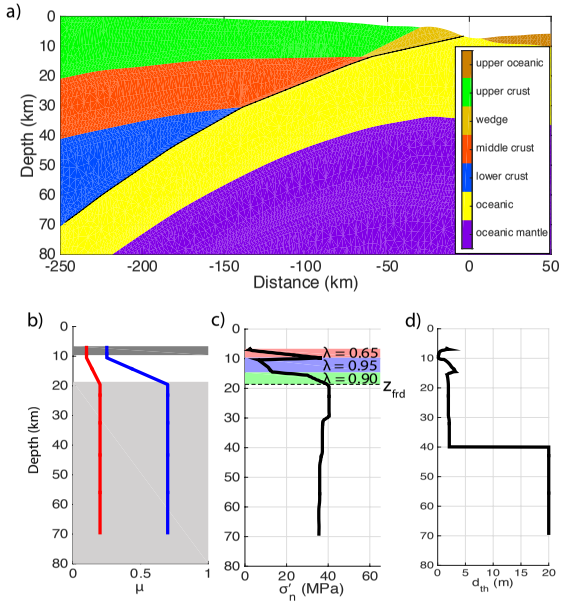

Figure 3
Click here to download Figure: fig3.eps

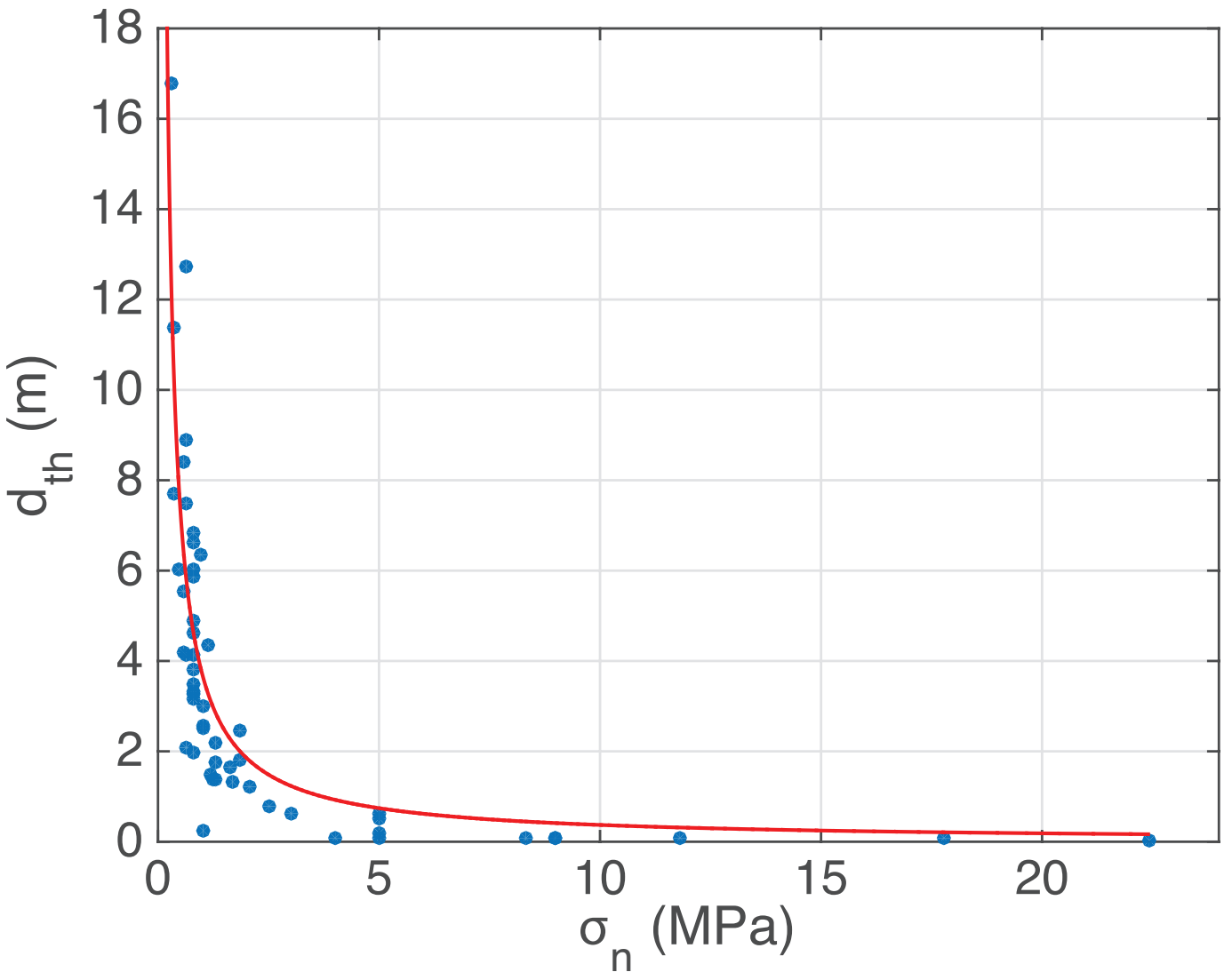

Figure 4
Click here to download Figure: fig4.eps

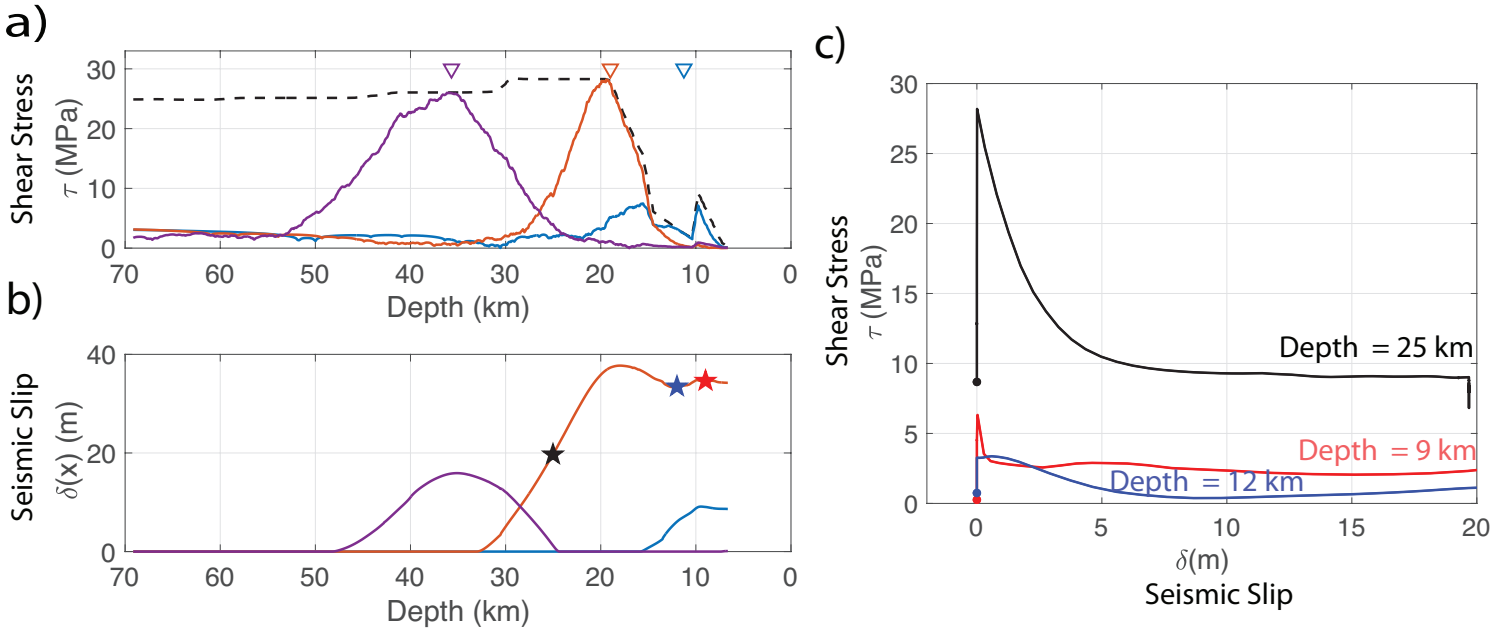

Figure 5
Click here to download Figure: fig5.pdf

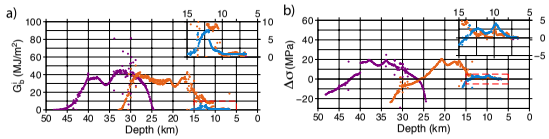

Figure 6
Click here to download Figure: fig6.eps

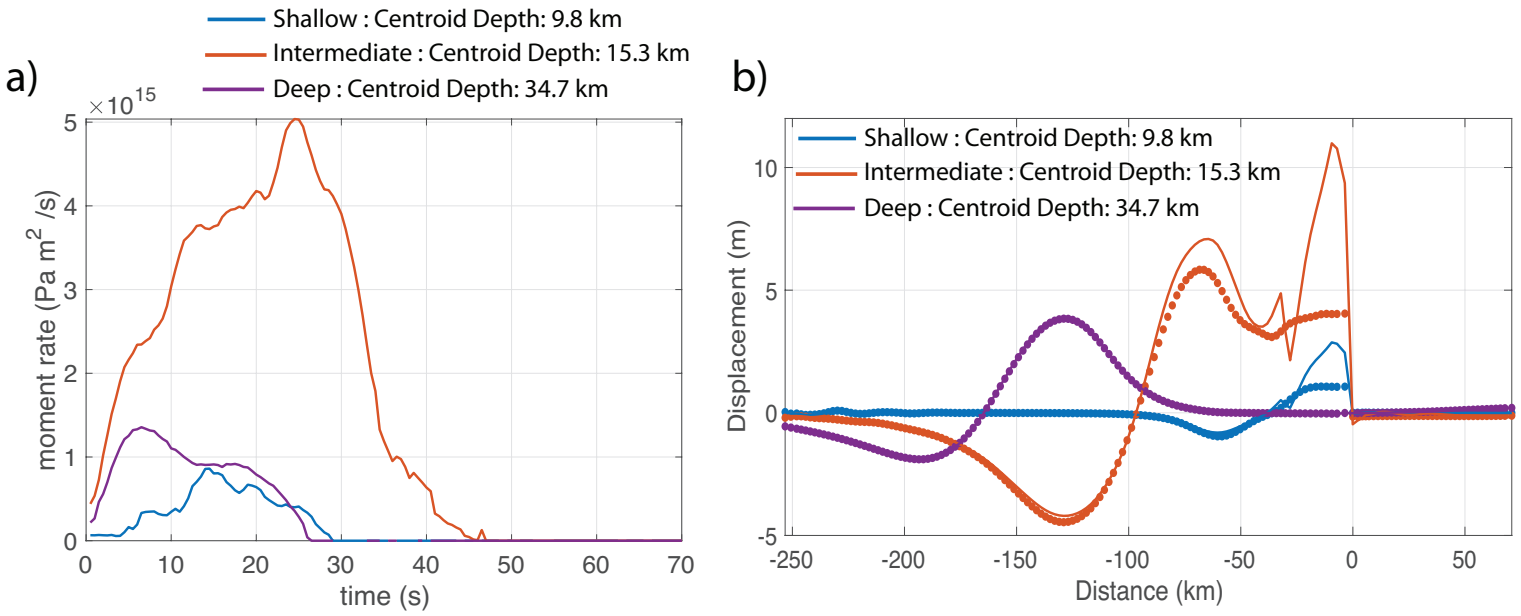

Figure 7
Click here to download Figure: fig7.eps

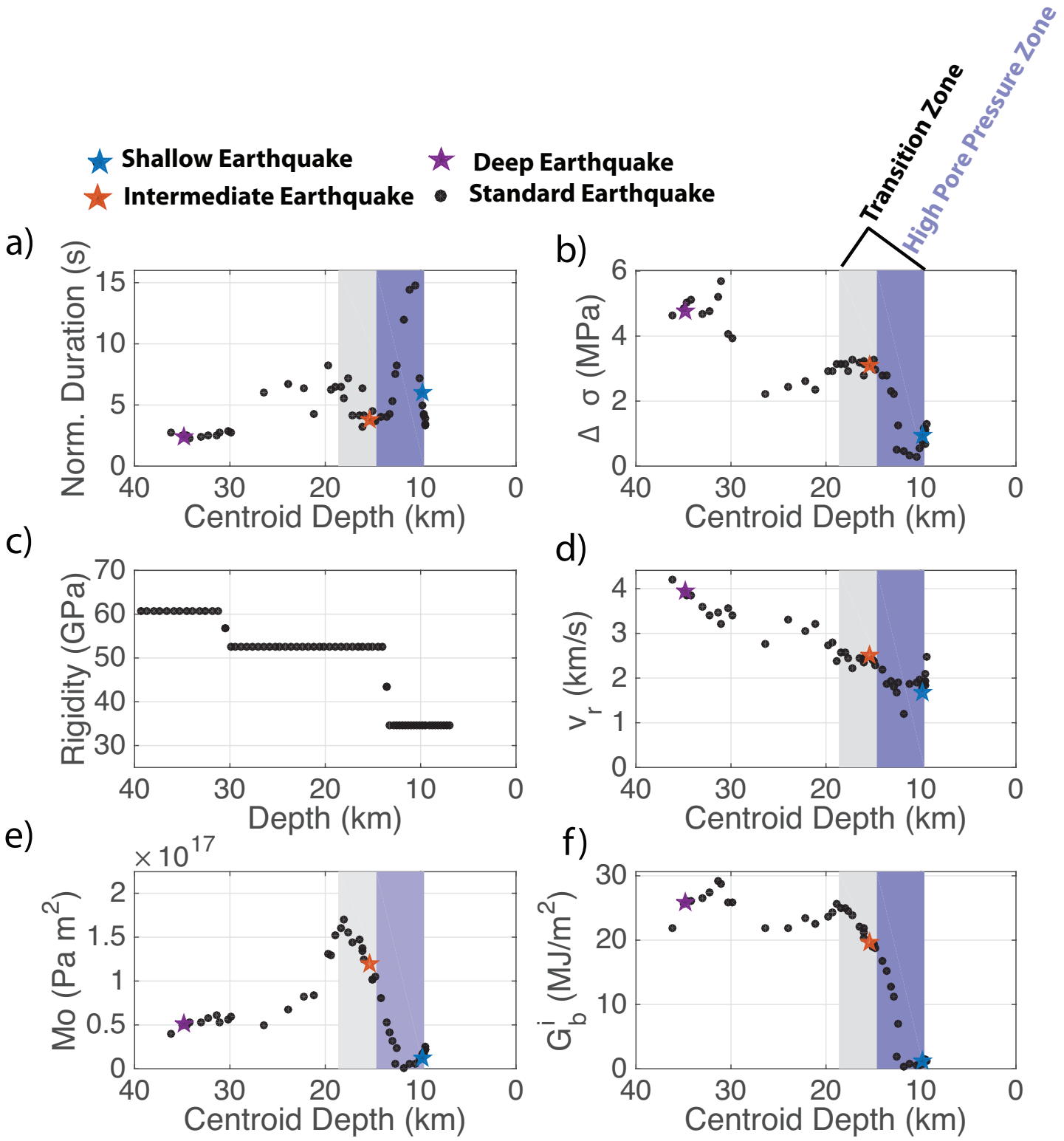

Figure 8
Click here to download Figure: fig8.pdf

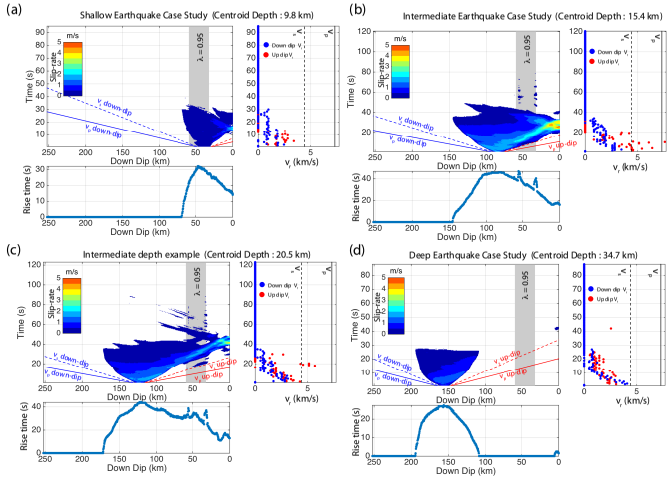

Figure 9
Click here to download Figure: fig9.eps

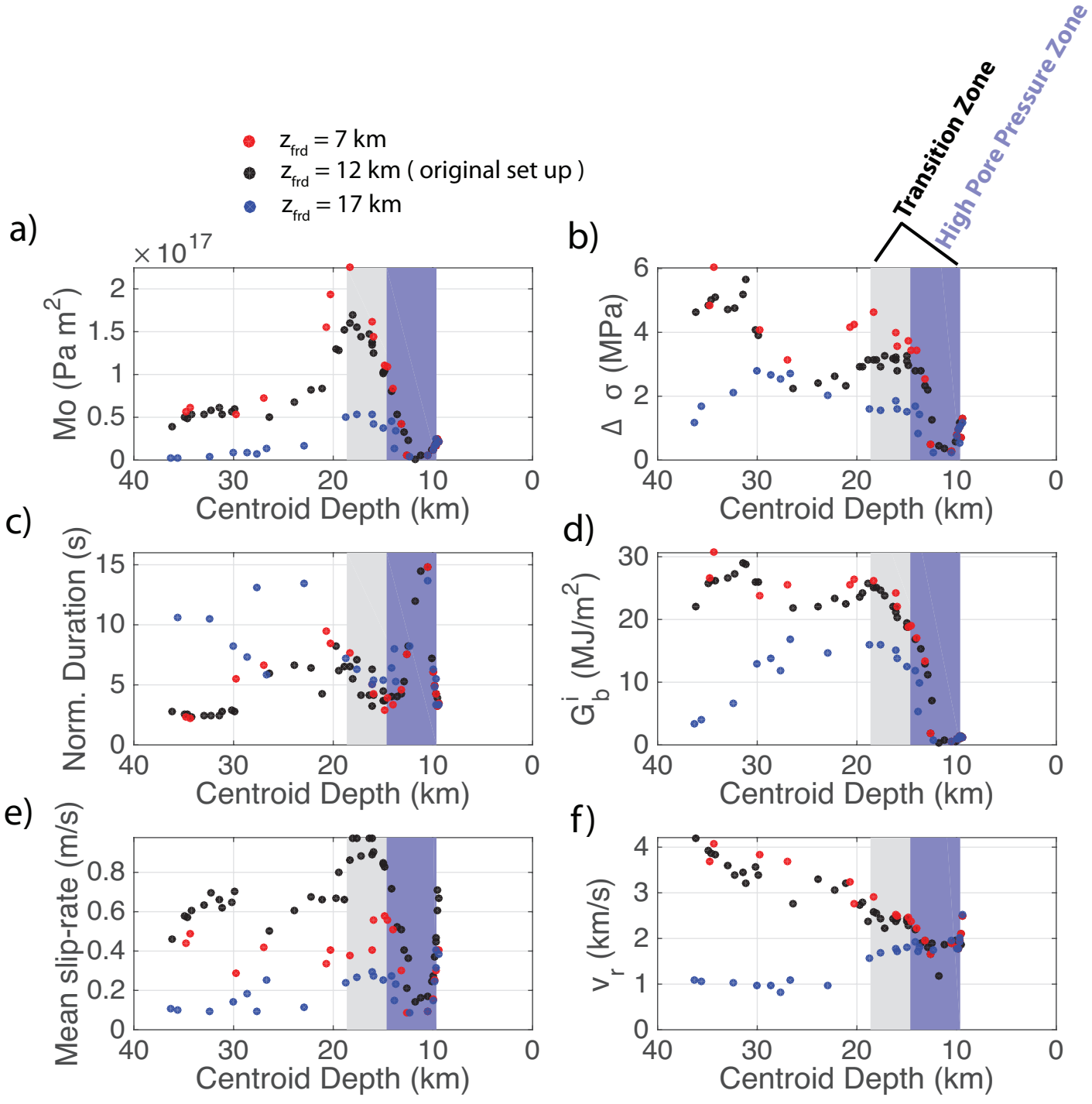

Figure 10
Click here to download Figure: fig10.eps